



## Superconductivity, superfluidity and quantum geometry in twisted multilayer systems

Päivi Törmä<sup>1</sup> , Sebastiano Peotta<sup>1</sup> and Bogdan A. Bernevig<sup>2,3,4</sup>

**Abstract** | Superconductivity has been observed in moiré systems such as twisted bilayer graphene, which host flat, dispersionless electronic bands. In parallel, theory work has discovered that superconductivity and superfluidity of flat-band systems can be made possible by the quantum geometry and topology of the band structure. These recent key developments are merging into a flourishing research topic: understanding the possible connection and ramifications of quantum geometry on the induced superconductivity and superfluidity in moiré multilayer and other flat-band systems. This article presents an introduction to how quantum geometry governs superconductivity and superfluidity in platforms including, and beyond, graphene. Ultracold gases are introduced as a complementary platform for quantum geometric effects and a comparison is made to moiré materials. An outlook sketches the prospects of twisted multilayer systems in providing the route to room-temperature superconductivity.

Superconductivity or superfluidity require bosonic particles to be in the same energy state; in the case of superconductors, these bosons are composites of two electrons, so-called Cooper pairs. However, being in the same state is not sufficient. The system needs to be able to host stable supercurrents, that is, dissipationless flow of particles: this is what makes superconductors useful in generating large magnetic fields or in providing qubits for quantum computing. The condensed matter community has long been exploring material candidates to bring superconductivity to room-temperature, high- $T_c$  materials such as cuprates leading the way<sup>1</sup>.

However, a complementary route towards high-temperature superconductivity has begun to emerge, that of purposefully designing materials less complex, and more tunable, than the traditional high- $T_c$  ones, following simple but fundamental theory guidelines relying on flat bands and quantum geometry. In moiré systems, such as twisted bilayer graphene (TBG), flattening of the electronic band structure occurs at certain twist angles. The discovery of correlated phases, including superconductivity, in TBG<sup>2–8</sup> thus suggests moiré systems as ideal platforms to explore the connection between flat-band superconductivity and quantum geometry.

In this Review, we introduce the essential theory of quantum geometry dependence of superfluidity and show how a finite Chern number of a band gives a fundamental lower bound of the flat-band superfluid weight, the observable that quantifies the ability of the system to support superfluid transport. We then explain

how a similar lower bound is given by a new type of zero-Chern-number topology in the context of TBG and review theory work that predicts the relevance of quantum geometric effects in the experimentally observed TBG superconductivity and other platforms, including ultracold gases. We conclude by discussing the prospects of reaching room-temperature superconductivity by band structure and topology design, and briefly refer to the exciting possibilities available for bosonic condensates of atoms, polaritons or photons in flat bands.

### Quantum geometry and flat-band superconductivity

The first theory suggestion for achieving high-temperature superconductivity is to use flat bands, where the energy dispersion as a function of momentum,  $\epsilon(\mathbf{k})$ , is constant. In flat bands, the critical temperature  $T_c$ , at which Cooper pairs form, is predicted<sup>9–11</sup> to be linearly proportional to the interaction  $U$  between the Cooper pair constituents for weak interactions. Comparison with the prediction of the Bardeen–Cooper–Schrieffer (BCS) theory of superconductivity<sup>12</sup> for dispersive bands,  $T_c \propto e^{-1/(n_F U)}$  ( $n_F$  is the density of states at the Fermi level), shows that the critical temperature is exponentially enhanced in flat-band systems compared with dispersive systems, in the BCS formalism. The enhancement is due to high density of states and dominance of interactions over kinetic energy. The band does not need to be exactly flat to benefit from this; any band where the interaction  $U$  is much larger than the bandwidth will do.

<sup>1</sup>Department of Applied Physics, Aalto University School of Science, Aalto, Finland.

<sup>2</sup>Department of Physics, Princeton University, Princeton, NJ, USA.

<sup>3</sup>Donostia International Physics Center, Donostia–San Sebastián, Spain.

<sup>4</sup>Ikerbasque, Basque Foundation for Science, Bilbao, Spain.

e-mail: [paivi.torma@aalto.fi](mailto:paivi.torma@aalto.fi)  
<https://doi.org/10.1038/s42254-022-00466-y>

**Key points**

- Bands of (quasi-)flat dispersion dramatically enhance Cooper pairing as their (nearly) vanishing kinetic energy allows interaction effects to dominate.
- Superfluidity and stable supercurrents are possible in a flat band if the band has non-trivial quantum geometry: the related overlap of the Wannier functions facilitates movement of interacting particles even when non-interacting particles would be localized.
- Twisted bilayer graphene exhibits nearly flat bands at its Fermi energy for small twist angles. Theory work suggests that quantum geometry is essential for the experimentally observed twisted bilayer graphene superconductivity and that a topological invariant called Euler class provides a lower bound for its superfluid weight.
- Ultracold gases offer another promising platform for highly controllable studies of superfluidity in moiré geometries. The first experiments are on the way.
- A flat-band dispersion together with a quantum geometry that guarantees superfluidity are powerful guidelines for the search of superconductivity at elevated temperatures.

A second guideline from theory, however, is needed, since the flat band provides only the critical temperature for Cooper pairing but does not determine whether superfluidity and supercurrents exist. Their existence is not obvious in a flat band: if non-interacting fermionic particles are localized on atomic sites and their ground state is an insulator, then no current is possible. Would interacting particles also just form localized pairs that cannot move? Or is supercurrent possible, and, if yes, under which general conditions? The answer was found only relatively recently: stable supercurrent and superfluidity are possible even in a flat band, if the band has non-trivial quantum geometry<sup>13–17</sup>. The quantum geometry here refers to distances and curvatures in the space (or manifold) formed by the electronic Bloch functions, that is, the eigenfunctions of the band.

The quantum geometry of a band is characterized by the quantum geometric tensor (QGT)<sup>18,19</sup>. The real part of the QGT is the quantum metric, which quantifies the amplitude distance between two close quantum states. However, quantum states also have a phase difference, leading to the definition of the Berry phase, which is the imaginary part of the QGT. Integrated over the Brillouin zone, the Berry curvature gives the Chern number — an integer — which is a topological invariant that changes only stepwise. Non-zero values of the quantum metric or of the Berry curvature make the quantum geometry of the system non-trivial. If the Chern number is non-zero, the system is also topologically non-trivial (BOX 1). The Berry curvature is known to be relevant for numerous physical phenomena, including topological insulators and superconductors<sup>20,21</sup>, while the importance of the quantum metric is only emerging — it turns out to be the quantity that governs flat-band superconductivity.

The underlying reason why quantum geometry is important for superconductivity and superfluidity is that it quantifies the overlap between the Wannier functions of a band. If the Wannier functions are very localized and do not overlap, the flat band is trivial and transport is not possible. Indeed, a trivial flat band is equivalent to an insulator in the atomic limit of large atom–atom separation. However, there are many systems where flat bands occur in conjunction with mobile electrons. Many lattice geometries, for example, the Lieb lattice, support eigenstates with opposite phases at nearby lattice sites,

so that tunnelling contributions from neighbouring sites interfere destructively. This leads to a set of degenerate eigenstates, forming a flat band (FIG. 1a). Another route to nearly flat bands are superlattices that introduce new, smaller Brillouin zones, and, consequently, new band gaps that then lead to band flattening (FIG. 1b).

Band-gap opening is given, in general, by the interference between a state of certain momentum and a backscattered state with opposite momentum. Therefore, both mechanisms of flat-band generation rely on the quantum interference of the wavefunctions. One is best illustrated in the real space and the other in the momentum space. Many types of lattices (such as line-graph lattices, split graph, Lieb<sup>22–24</sup>) can support flat bands that result from wavefunction interference. A large number of so-obtained flat bands are topological in origin<sup>25</sup> and exhibit non-zero (non-Abelian) Berry curvature. Whether or not adding interaction to these bands leads to transport and supercurrent depends on the overlap of the Wannier functions, that is, the Fourier transforms of the Bloch functions (FIG. 2). The overlap, in turn, is governed by quantum geometry. This explains the quantum geometric origin of flat-band superconductivity.

In the quest for room-temperature superconductivity, one therefore needs to design not only the band dispersion but also the properties of the Bloch functions, that is, the band geometry and topology. TBG and other moiré materials, where a superlattice is created by a twist angle between two graphene layers, offer excellent potential for flat-band engineering and control<sup>4–8</sup>. At about one degree, the so-called first magic angle, a set of flat bands appears in the electronic spectrum. The individual graphene sheets have finite Berry curvatures near the four Dirac points of TBG (two per layer, located at the  $K$  and  $K'$  high-symmetry points of the Brillouin zone, called valleys). Interlayer hopping of electrons couples the Dirac points of the same valley and Berry curvature (also called ‘helicity’ here) in the two layers. In contrast, the different valleys are decoupled. The coupling of the same valley and same helicity Dirac nodes, with their additive helicity, leads to the emergence of a new type of topology of the single-valley model of TBG. Further degrees of freedom in the design of bands and their topology are given by stacking more than two graphene layers or creating moiré materials composed of elements other than carbon. Quantum gases of ultracold atoms form another playground for the study of interacting flat bands. In these systems, one can create moiré geometries as well as simpler flat-band systems, such as Lieb and kagome lattices, and tune the interparticle interaction over a wide range from repulsive to attractive.

### The quantum geometric contribution of superfluid weight

**Superfluid weight.** The electrodynamic properties of superconducting materials are captured by the constitutive relation (in the London gauge)<sup>12,26</sup>

$$\mathbf{j} = -D_s \mathbf{A}, \quad (1)$$

with  $\mathbf{j}$  the current density,  $\mathbf{A}$  the vector potential and  $D_s$  the superfluid weight. In tandem with Maxwell’s

**Box 1 | Band-structure invariants and topology**

The eigenfunctions of a Bloch band, describing electrons in crystalline materials, take the generic form  $|\psi_{nk}\rangle = e^{ik \cdot r} |u_{nk}\rangle$ , where  $n$  denotes the band number and  $|u_{nk}\rangle$  is the periodic Bloch function, since it has the same periodicity as the crystalline lattice. They are defined up to a  $\mathbf{k}$ -dependent phase and can enter the expression of an observable quantity only through band-structure invariants, which do not depend on how this phase is chosen (called a gauge choice).

A basic invariant is the quantum geometric tensor (QGT)

$$\mathcal{B}_{ij}(\mathbf{k}) = 2\text{Tr}[P(\mathbf{k})\partial_i P(\mathbf{k})\partial_j P(\mathbf{k})]. \quad (22)$$

It is expressed in terms of the projector to the band  $n$  of interest,  $P(\mathbf{k}) = |u_{nk}\rangle \langle u_{nk}|$ , which is unchanged under the gauge transformation  $|u_{nk}\rangle \rightarrow e^{i\theta(\mathbf{k})} |u_{nk}\rangle$ . Importantly, the QGT is a Hermitian matrix with non-negative eigenvalues, i.e. a positive semi-definite complex matrix. A positive semi-definite complex matrix  $A_{ij}$  has the property that  $\sum_j b_i^* A_{ij} b_j \geq 0$  for arbitrary complex numbers  $b_i$ .

Using  $P(\mathbf{k}) = P^\dagger(\mathbf{k}) = P^2(\mathbf{k})$ , the real part of the QGT can be written as

$$g_{ij}(\mathbf{k}) = \text{Re } \mathcal{B}_{ij}(\mathbf{k}) = \text{Tr}[\partial_i P(\mathbf{k})\partial_j P(\mathbf{k})] \quad (23)$$

and is known as the quantum metric (or Fubini–Study metric). It is a measure of the distance between infinitesimally close wavefunctions in  $\mathbf{k}$ -space. The quantum metric appears also as the gauge-invariant part of the Marzari–Vanderbilt localization functional for Wannier functions.

The imaginary part of the QGT is related to the concept of Berry (geometric) phase. Let us first remind ourselves about the Berry connection in band  $n$

$$\mathbf{A}(\mathbf{k}) = i\langle u_{nk} | \nabla_{\mathbf{k}} u_{nk} \rangle. \quad (24)$$

The Berry phase can be expressed as an integral over a surface  $S$  whose boundary is a closed curve  $\gamma = \partial S$

$$\Phi_{\text{Berry}} = \int_S d\mathbf{S} \cdot \nabla_{\mathbf{k}} \times \mathbf{A}(\mathbf{k}) = \frac{1}{2} \int_S dS_i \epsilon^{lmn} \text{Im } \mathcal{B}_{nm}(\mathbf{k}). \quad (25)$$

The quantity  $\nabla_{\mathbf{k}} \times \mathbf{A}(\mathbf{k})$ , which is proportional to the imaginary part of the QGT, is known as the Berry curvature. If in the above equation the integral is extended to the whole Brillouin zone (assuming dimension  $d=2$ ), one obtains the Chern number, a topological invariant,

$$\mathcal{C} = \frac{1}{2\pi} \int_{\text{BZ}} d^2k \text{Im } \mathcal{B}_{12}(\mathbf{k}). \quad (26)$$

The Chern number can take only integer values.

The fact that the QGT is positive semi-definite implies that the real and imaginary parts satisfy a number of constraints, of which Eq. (17) is an example. The Berry connection  $\mathbf{A}(\mathbf{k})$  and curvature can be generalized to the case of multiple bands ( $\mathbf{A}^{mn}(\mathbf{k}) = i\langle u_{mk} | \nabla_{\mathbf{k}} u_{nk} \rangle$ ), in which case they are called non-Abelian and bring about a wide array of new topological invariants. One example is the Euler class  $e_2$ , a topological invariant expressed in terms of the non-Abelian Berry curvature. In systems with  $C_{2z}T$  symmetry, the non-Abelian Berry connection and curvature of two bands can be written as  $\mathbf{A}(\mathbf{k}) = -\mathbf{a}(\mathbf{k})\sigma_y$  and  $\mathcal{F}_{xy}(\mathbf{k}) = -f_{xy}(\mathbf{k})\sigma_y$ , respectively ( $\sigma_y$  is a Pauli matrix). The Euler class  $e_2$  is the invariant defined as

$$e_2 = \frac{1}{2\pi} \int d^2k f_{xy}. \quad (27)$$

The abelian QGT in Eq. (22) is the trace of a more general, positive-definite non-Abelian QGT (matrix)  $\mathfrak{G}_{ij}$ : if the Bloch states for  $n=1,\dots,N$  bands are written as a vector  $u(\mathbf{k}) = (|u_{1\mathbf{k}}\rangle, \dots, |u_{N\mathbf{k}}\rangle)$ , the non-Abelian QGT is  $\mathfrak{G}_{ij} = \partial_i u^\dagger (1 - uu^\dagger) \partial_j u$  and  $\mathcal{B}_{ij} = \text{Tr}[\mathfrak{G}_{ij}]$ .

equations, Eq. (1) provides a quantitative description of the phenomena of perfect conductivity and perfect diamagnetism (Meissner effect), therefore, a non-zero superfluid weight  $D_s \neq 0$  is the very criterion of superconductivity<sup>27,28</sup>. The superfluid weight also measures the energy required to create a modulation of the phase  $\phi(\mathbf{r})$  of the superconducting order parameter  $\psi(\mathbf{r}) = |\psi(\mathbf{r})|e^{i\phi(\mathbf{r})}$ , since the free energy contains the term

$$\Delta F = \frac{\hbar^2}{2e^2} \int d^d\mathbf{r} \sum_{ij=x,y,z} D_{s,ij} \partial_i \phi(\mathbf{r}) \partial_j \phi(\mathbf{r}), \quad (2)$$

with  $d=2,3$  the spatial dimension,  $\hbar$  Planck's constant and  $e$  the electron charge. In anisotropic systems, the superfluid weight is not a scalar but a rank-2 tensor  $D_{s,ij}$  and Eq. (1) is modified accordingly.

The superfluid weight of a spinful electron band at zero temperature given by single-band BCS theory is<sup>12,29</sup>

$$D_{s,ij} = \frac{e^2}{\hbar^2} \int \frac{d^d\mathbf{k}}{(2\pi)^d} f(\varepsilon(\mathbf{k})) \frac{\partial^2 \varepsilon(\mathbf{k})}{\partial k_i \partial k_j}, \quad (3)$$

where  $\varepsilon(\mathbf{k})$  is the dispersion of the band. Here and in the following, quasimomentum  $\mathbf{k}$  integrals are performed over the first Brillouin zone. The function  $f(\varepsilon)$  is the occupation of a single-particle state with energy  $\varepsilon$  in the BCS ground state<sup>12,26</sup>. By assuming an approximately parabolic band  $\varepsilon(\mathbf{k}) \approx \hbar^2 \mathbf{k}^2 / (2m_{\text{eff}})$ , one obtains  $D_s = e^2 n / m_{\text{eff}}$  where  $n$  is the total number density and  $m_{\text{eff}}$  is the particle effective mass<sup>30</sup>. At finite temperature, only a fraction of the charge carriers participate in superfluid transport, thus, the superfluid weight reads  $D_s = e^2 n_s / m_{\text{eff}}$  where  $n_s$  is the superfluid density and  $0 \leq n_s/n \leq 1$  the corresponding superfluid fraction<sup>12,26,31</sup>. In the extreme limit in which the single-particle effective mass is very large or even diverging, the superfluid weight should be very small or even vanishing according to Eq. (3) (REF.<sup>32</sup>). To best understand why this is not generally the case in multiband systems, it is illuminating to first consider the two-body problem in a flat band<sup>16</sup>.

**Geometric origin of the pair effective mass in a flat band.**

The Fermi sea is unstable and forms pairs under an arbitrarily small attractive interaction between electrons<sup>12</sup>. In three dimensions, the strength of a short-range attractive interaction needs to be larger than a threshold for two quantum particles to form a bound state; therefore, the existence of the Fermi sea is needed for forming pairs with arbitrarily small interactions. On the contrary, in the limit of infinite effective mass, that is, in a flat band, a bound state of two quantum particles is always present for any small value of the attractive interaction strength<sup>16</sup>. A crucial question is: what is the effective mass of the bound state? Naively, one could expect that, since the constituent particles have infinite effective mass, this would also be the case for the bound state they form. This would mean that the superfluid weight is zero and no superconducting state can occur in a partially filled flat band. However, one can show that the bound state can disperse as a result of interactions<sup>16</sup>.

To illustrate this important point, we consider a generic lattice model with Hamiltonian

$$\hat{H} = \hat{H}_0 + \hat{H}_{\text{int}} \quad (4)$$

and introduce some definitions. The term

$$\hat{H}_0 = \sum_{i\alpha, j\beta} \sum_{\sigma} \hat{c}_{i\alpha}^\dagger K_{i\alpha, j\beta}^{\sigma} \hat{c}_{j\beta}^{\sigma} \quad (5)$$

describes the single-particle hopping between the lattice sites. The hopping amplitudes  $K_{i\alpha, j\beta}^{\sigma}$  and the fermionic

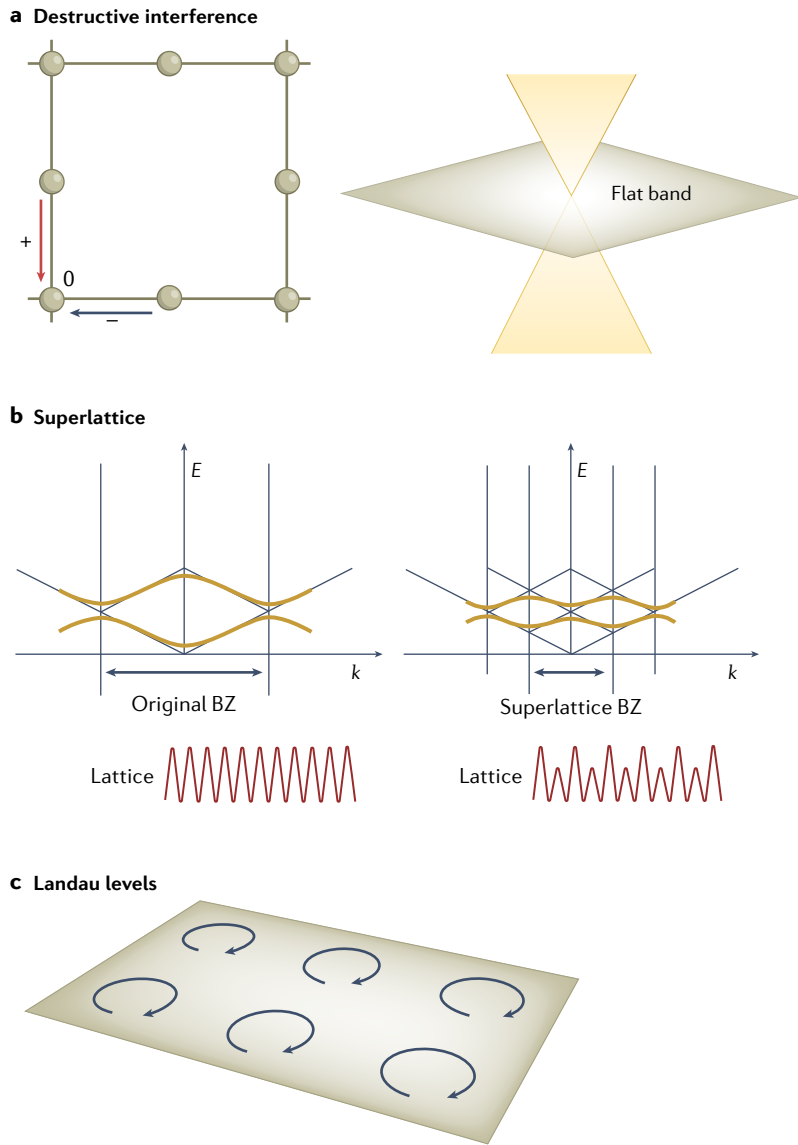


**Fig. 1 | Formation of flat bands.** **a** Certain lattice geometries, such as the Lieb lattice (left), support eigenstates that occupy a subset of lattice sites. The phases of the wavefunction are such that tunnelling to the rest of the sites is impossible due to destructive interference, leading to localized states and a flat band (right). **b** By introducing a superlattice on top of a periodic system, a Brillouin zone (BZ) smaller than the original emerges, and if new band gaps are opened, band flattening takes place. **c** Landau levels are a well-known example of a flat-band system. One can understand the localization and band flattening via plaquettes (closed loops) with winding phases so that interference prevents movement, or, alternatively, one may think of the plaquettes as forming a larger unit cell and a superlattice.

field operators  $\hat{c}_{i\alpha\sigma}$  are labelled by the unit cell index  $\mathbf{i}=(i_1, i_2, i_3)$  and the sublattice (orbital) index  $\alpha=1, \dots, N_{\text{orb}}$  ( $N_{\text{orb}}$  is the number of orbitals in a unit cell), while  $\sigma=\uparrow, \downarrow$  is the spin index. For concreteness, we focus on an interaction term of the Hubbard form

$$\hat{H}_{\text{int}} = -U \sum_{i\alpha} \hat{c}_{i\alpha\uparrow}^\dagger \hat{c}_{i\alpha\uparrow} \hat{c}_{i\alpha\downarrow}^\dagger \hat{c}_{i\alpha\downarrow} \quad (6)$$

where  $U > 0$ . Due to translational symmetry ( $K_{i\alpha,j\beta}^\sigma = K_{\alpha,\beta}^\sigma(\mathbf{i} - \mathbf{j})$ ), the single-particle band dispersions  $\varepsilon_{n\mathbf{k}\sigma}$  and periodic Bloch functions  $|u_{n\mathbf{k}\sigma}\rangle$  are obtained from the eigenvalue equation

$$\tilde{K}^\sigma(\mathbf{k})|u_{n\mathbf{k}\sigma}\rangle = \varepsilon_{n\mathbf{k}\sigma}|u_{n\mathbf{k}\sigma}\rangle, \quad (7)$$

with  $\tilde{K}^\sigma(\mathbf{k})$  the Fourier transform of the hopping matrix  $K^\sigma$  (REF. <sup>13</sup>). We also assume time-reversal symmetry  $K_{i\alpha,j\beta}^\sigma = (K_{j\alpha,i\beta}^\sigma)^*$  and define  $u_{n\mathbf{k}}(\alpha) \equiv u_{n\mathbf{k}\uparrow}(\alpha) = u_{n,-\mathbf{k},\downarrow}^*(\alpha)$  and  $\varepsilon_{n\mathbf{k}} \equiv \varepsilon_{n\mathbf{k}\uparrow} = \varepsilon_{n,-\mathbf{k},\downarrow}$ . In the following, we always use Greek letters  $\alpha$  and  $\beta$  to label the sublattices, while Latin letters  $m$  and  $n$  are band labels.

From the solution of the two-body problem in a flat band (labelled by  $\bar{n}$ ), it has been shown that the effective mass of the bound state is given approximately by

$$\begin{aligned} \left[ \frac{1}{m_{\text{eff}}} \right]_{ij} &\approx \frac{U\Omega_c}{\hbar^2} \int \frac{d^d\mathbf{k}}{(2\pi)^d} \sum_{\alpha=1}^{N_{\text{orb}}} \partial_i P_{\alpha\alpha}(\mathbf{k}) \partial_j P_{\alpha\alpha}(\mathbf{k}) \\ &\approx \frac{U\Omega_c}{N_{\text{orb}}\hbar^2} \int \frac{d^d\mathbf{k}}{(2\pi)^d} g_{jl}(\mathbf{k}) \end{aligned} \quad (8)$$

where  $\Omega_c$  is the unit cell volume,  $\partial_i \equiv \partial_{k_i}$  and  $P_{\alpha\beta}(\mathbf{k}) = u_{\bar{n}\mathbf{k}}(\alpha) u_{\bar{n}\mathbf{k}}^*(\beta)$  are the matrix elements of the band projector  $P(\mathbf{k}) = |u_{\bar{n}\mathbf{k}}\rangle \langle u_{\bar{n}\mathbf{k}}|$  of the flat band, an  $N_{\text{orb}} \times N_{\text{orb}}$  matrix<sup>16</sup>. The quantity  $g_{jl}(\mathbf{k})$  is the quantum metric (BOX 1). Equation (8) shows that the effective mass of a two-body state in a flat band depends on both the interaction strength and the quantum metric, a single-particle property.

This result demonstrates that Cooper pairs can have a finite effective mass and, thus, support transport if the flat-band quantum metric is non-zero. This is in sharp contrast with Eq. (3), which gives zero superfluid weight for a partially filled single (or non-hybridizing) flat band, showing that Eq. (3) neglects additional contributions that come into play in the case of multiband/multiorbital lattices ( $N_{\text{orb}} > 1$ ). These were identified only recently by applying standard BCS theory to multiband lattice models<sup>13–15</sup>.

**Conventional and geometric contributions of the superfluid weight.** The superfluid weight is a static transport coefficient defined as<sup>28</sup>

$$D_{s,jl} = -\lim_{\mathbf{q}_\parallel \rightarrow 0} \chi_{jl}(q_\parallel=0, \mathbf{q}_\perp, \omega=0), \quad (9)$$

where  $\chi_{jl}(\mathbf{q}, \omega)$  is a response function, that of the current induced in the system to linear order in the vector potential  $\mathbf{A}$ . The vector potential enters the single-particle Hamiltonian  $\hat{H}_0$  by the usual Peierls substitution<sup>28</sup>. In the above equation, the wavevector  $\mathbf{q} = q_\parallel \hat{\mathbf{l}} + \mathbf{q}_\perp$  is decomposed into the collinear ( $q_\parallel$ ) and perpendicular ( $\mathbf{q}_\perp$ ) components with respect to the  $l=x, y, z$  axis (note that  $l$  is the second index appearing in  $D_{s,jl}$  and  $\chi_{jl}$ ).

To evaluate Eq. (9), it is necessary to resort to approximations. The typical BCS approximation is to replace the Hubbard interaction term by<sup>12,13</sup>

$$\hat{H}_{\text{int}} \approx \hat{H}_{\text{int}}^{(\text{m.f.})} = \sum_{i\alpha} (\Delta_\alpha \hat{c}_{i\alpha\uparrow}^\dagger \hat{c}_{i\alpha\downarrow}^\dagger + \text{H.c.}). \quad (10)$$

The pairing field  $\Delta_\alpha$  is independent of the unit cell index  $i$  since translational symmetry is assumed and is calculated self-consistently as  $\Delta_\alpha = -U \langle \hat{c}_{i\alpha\downarrow} \hat{c}_{i\alpha\uparrow} \rangle$ , where the

expectation value is taken with respect to the mean-field Hamiltonian  $\hat{H}_{\text{m.f.}} = \hat{H}_0 + \hat{H}_{\text{int}}^{(\text{m.f.})}$ .

For illustration purposes, we consider the case in which time-reversal symmetry is present and the pairing field is real for small vector potentials (see REF.<sup>17</sup> for the general case) and orbital-independent  $\Delta_\alpha = \Delta$  (see REF.<sup>33</sup> for a justification of orbital independence). Under these assumptions, the superfluid weight can be written as the sum of two terms  $D_s = D_{\text{conv}} + D_{\text{geom}}$  (REFS<sup>13,15</sup>). The first term reads

$$D_{\text{conv},jl} = \frac{e^2}{\hbar^2} \int \frac{d^d k}{(2\pi)^d} \sum_n \left[ -\frac{\beta}{2\cosh^2(\beta E_{nk}/2)} \right. \\ \left. + \frac{\tanh(\beta E_{nk}/2)}{E_{nk}} \right] \frac{\Delta^2}{E_{nk}^2} \partial_j \varepsilon_{nk} \partial_l \varepsilon_{nk}, \quad (11)$$

and is called the conventional contribution to the superfluid weight, since it is the sum over all bands of the result for the superfluid weight of a single-band model (Eq. (3)) (now at finite temperature  $T$ ,  $\beta^{-1} = k_B T$ , where  $k_B$  is the Boltzmann constant). In Eq. (11),  $E_{nk} = \sqrt{(\varepsilon_{nk} - \mu)^2 + \Delta^2}$  are the quasiparticle excitation energies of  $\hat{H}_{\text{m.f.}}$ .

The second term is called the geometric contribution to the superfluid weight

$$D_{\text{geom},jl} = \frac{e^2 \Delta^2}{\hbar^2} \int \frac{d^d k}{(2\pi)^d} \sum_{n \neq m} \left[ \frac{\tanh(\beta E_{nk}/2)}{E_{nk}} \right. \\ \left. - \frac{\tanh(\beta E_{mk}/2)}{E_{mk}} \right] \frac{(\varepsilon_{nk} - \varepsilon_{mk})^2}{E_{mk}^2 - E_{nk}^2} \\ \times (\langle \partial_j u_{nk} | u_{mk} \rangle \langle u_{mk} | \partial_l u_{nk} \rangle + (j \leftrightarrow l)). \quad (12)$$

This contribution is a qualitatively new feature of multiband/multiorbital lattice models and is associated to off-diagonal matrix elements of the current operator, which are proportional to

$$\langle u_{mk} | \nabla_k \tilde{K}^\dagger(k) | u_{nk} \rangle = \nabla_k \varepsilon_{nk} \delta_{n,m} \\ + (\varepsilon_{nk} - \varepsilon_{mk}) \langle u_{mk} | \nabla_k u_{nk} \rangle. \quad (13)$$

Indeed, the diagonal term  $\propto \nabla_k \varepsilon_{nk}$  leads to the conventional contribution Eq. (11) and the off-diagonal term  $\propto \langle u_{mk} | \nabla_k u_{nk} \rangle$  leads to the geometric contribution Eq. (12). Further details are given in REFs<sup>13,15,17</sup> and the review of REF<sup>34</sup>.

It is instructive to investigate the two contributions Eqs (11) and (12) in the isolated band limit, when the chemical potential is such that a single band, denoted by  $\bar{n}$ , is partially filled and other bands are separated from it by a large band gap  $E_{\text{gap}}$

$$|\varepsilon_{mk} - \varepsilon_{\bar{n}k}| \gtrsim E_{\text{gap}} \gg \Delta \quad \text{for } m \neq \bar{n}. \quad (14)$$

The conventional contribution in this case is just Eq. (3) with  $\varepsilon(k)$  replaced by  $\varepsilon_{\bar{n}k}$ . On the other hand, care is required for the computation of the geometric contribution. One might expect that the geometric contribution should be vanishing in this limit since the terms of the response function that are off-diagonal in band space are suppressed by the factor  $E_{mk} - E_{\bar{n}k} \gtrsim E_{\text{gap}}$ , with  $m \neq \bar{n}$ , at the denominator. This would be incorrect because the off-diagonal terms of the current operator are proportional to the band gap, as seen from Eqs (13) and (14). A careful analysis<sup>15</sup> shows that the geometric

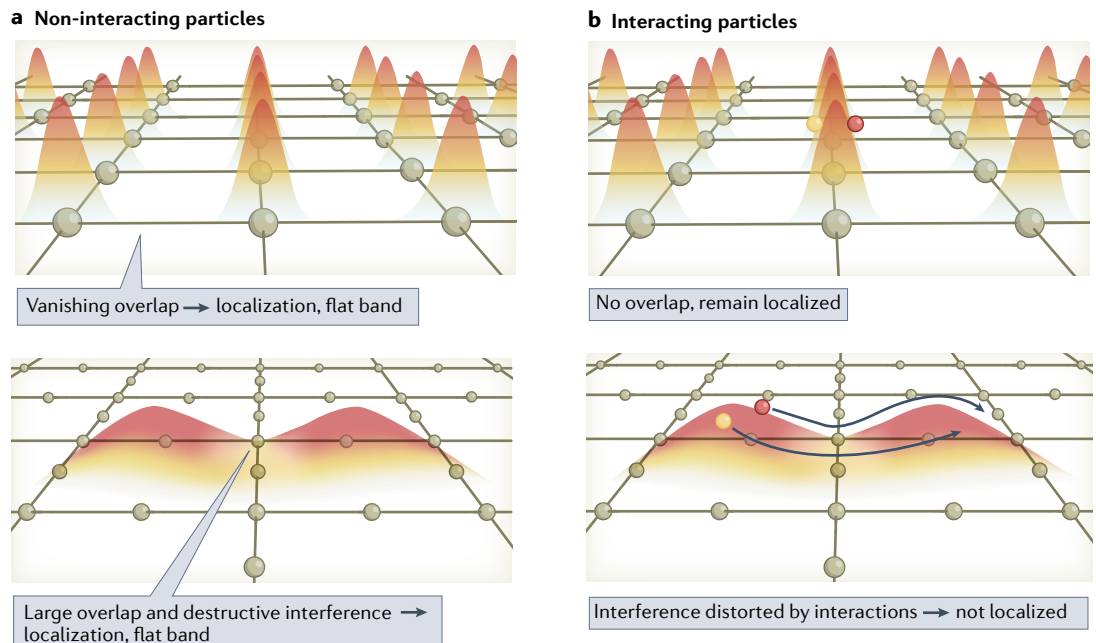


**Fig. 2 | Role of Wannier function overlap in flat-band superfluidity.** **a** Non-interacting particles can be immobile either if their Wannier functions are exponentially localized at the lattice sites (top) or due to destructive interference of overlapping Wannier functions (bottom). **b** Interacting particles with localized Wannier functions are also immobile (top). However, if there is a finite overlap of Wannier functions, interactions distort the interference and the particles can move (bottom). Wannier function overlaps are controlled by the quantum geometry of the band; in particular, topological systems cannot have exponentially localized Wannier functions.

contribution is non-zero even in the isolated band limit and, somewhat counter-intuitively, can be expressed purely in terms of quantities relative to the partially filled band, in particular, its quantum metric. This is most clearly illustrated in the case of an isolated flat band, where one obtains ( $\nu$  is the band filling)<sup>13</sup>

$$D_{s,jl} = D_{\text{geom},jl} = \frac{4e^2 \Delta \sqrt{\nu(1-\nu)}}{\hbar^2} \int \frac{d^d k}{(2\pi)^d} g_{jl}(k), \quad (15)$$

which relates the superfluid weight to the quantum metric  $g_{jl}(k)$  integrated over the Brillouin zone. In the general case, when  $\Delta$  is not necessarily real for all vector potentials,  $g_{jl}$  is replaced by the minimal quantum metric<sup>17</sup>. It is clear by comparing Eq. (15) with Eq. (8) that, with some minor approximations, the non-zero superfluid weight in the flat-band limit can be entirely explained in terms of the two-body bound state effective mass<sup>16,35</sup>. The geometric contribution scales with the superconducting energy gap  $\Delta \propto U$ , while the conventional contribution scales roughly with the Fermi energy  $E_F$ , which is on the order of the bandwidth of the partially filled band. In usual superconductors (without flat bands), the gap  $\Delta$  is generally a much smaller energy scale than the Fermi energy and the geometric contribution is rather small.

Only very recently have physical systems in which the electronic bandwidth is comparable with the superconducting gap been realized in the laboratory, in particular, magic-angle TBG<sup>36</sup>. The essential role of the off-diagonal matrix elements of the current operator was pointed out in 1995 (REF.<sup>37</sup>) in the case of the exciton superfluid phase occurring in quantum Hall bilayers, which can be considered the first example of a flat-band superfluid observed experimentally. Moreover, it was theoretically shown that the superfluid weight is non-zero in the case of the flat band of surface states present in rhombohedral graphene<sup>38</sup>. However, these have apparently been regarded as system-specific findings until general results connecting superfluidity with quantum geometry, such as Eqs (12) and (15), were obtained<sup>13,15</sup>.

**Wannier function overlap and topological lower bound for supercurrent.** A natural question raised by Eq. (15) is what property of the flat-band wavefunctions is captured by the quantum metric and why it affects transport and superfluidity. The physical interpretation of the quantum metric can be most easily provided by Wannier functions, that is, Fourier transforms of the Bloch states

$$w_n(i, \alpha) = \frac{\Omega_c}{(2\pi)^2} \int d^d k e^{ik \cdot r_i} u_{n\mathbf{k}}(\alpha). \quad (16)$$

A common prescription to choose a gauge for the Wannier functions is the one based on the Marzari–Vanderbilt localization functional, whose minimization leads to the maximally localized Wannier functions<sup>39</sup>. The gauge-invariant part of the localization functional is the trace of the quantum metric integrated over the Brillouin zone, which sets a lower bound on how much the Wannier functions can be localized. It was shown in REF.<sup>33</sup> that a flat-band superconductor can be described by an effective spin Hamiltonian whose exchange

couplings are controlled by the overlap of the Wannier functions, which, in turn, is related to the Marzari–Vanderbilt functional and, thus, to the quantum metric. This provides a solid basis for the interpretation of the quantum metric as an invariant measure of the overlap/spread of the flat-band wavefunctions.

Topological invariants that describe the electronic band structure provide an obstruction to the full localization of Wannier functions. An important topological invariant is the Chern number,  $C$  (REF.<sup>40</sup>) (BOX 1). From the positive semi-definiteness of the QGT, one obtains the inequality

$$\det \mathcal{M}^R \geq C^2, \quad \text{with } \mathcal{M}_{ij}^R = \frac{1}{2\pi} \int d^2 k g_{ij}(k). \quad (17)$$

Hence, a non-zero Chern number also bounds the superfluid weight, since the matrix  $\mathcal{M}^R$  is precisely the integrated quantum metric that enters in Eq. (15). This is explained by the fact that, if the Chern number is non-zero, one cannot find exponentially localized Wannier functions<sup>41,42</sup>; at best, the Wannier states are algebraically decaying with a known exponent  $1/r^2$  (REF.<sup>43</sup>). Such wavefunctions are necessarily overlapping and, thus, are expected to support a robust superfluid state in the isolated flat-band limit. Equation (15) assumes time-reversal symmetry and is bounded by the spin Chern number. For the possibility of topological lower bounds in the absence of time-reversal symmetry, see REF.<sup>17</sup>. The Marzari–Vanderbilt localization functional and the quantum metric also appear in an upper bound for the superfluid weight, derived without the use of a mean-field approximation<sup>44</sup>.

Inequalities similar to Eq. (17) have been discovered in the case of two more topological invariants: the winding number in  $d=1$  (REF.<sup>33</sup>) and the Euler class in  $d=2$  (REF.<sup>45</sup>), which is relevant for magic-angle TBG. One expects such bound identities to exist for every topologically non-trivial band. Topology is a sufficient but not necessary condition for non-zero superfluid weight<sup>14</sup> because the quantum metric can be non-zero for zero Chern number and even zero Berry curvature bands — a bound that also describes such bands was recently defined using obstructed Wannier centres<sup>46</sup>.

**BKT temperature of superconductivity in a flat band.** The superfluid weight controls the susceptibility of the order parameter phase to thermal fluctuations, as seen from Eq. (2), and, thus, it is expected to affect the critical temperature of superconductivity. However, this effect is not captured by BCS theory in its simplest form, since the order parameter  $\Delta(\mathbf{r})$  is a non-fluctuating quantity at the mean-field level. In  $d=2$ , the relation between critical temperature and superfluid weight can be made precise thanks to the universal relation  $T_{\text{BKT}} = \frac{\pi\hbar^2}{8e^2} D_s(T_{\text{BKT}})$  (REF.<sup>47</sup>), where  $T_{\text{BKT}}$  is the Berezinskii–Kosterlitz–Thouless (BKT) temperature, that is, the critical temperature of a two-dimensional superfluid, and  $D_s(T_{\text{BKT}})$  is the superfluid weight slightly below the same temperature. For an isolated flat band, one obtains  $T_{\text{BKT}} \sim U$  (REFS<sup>13,15</sup>) for weak interactions, that is, the same linear dependence on  $U$  as for the BCS critical temperature in a flat band. The BKT temperature saturates for an interaction strength on

the order of the band gap  $U \sim E_{\text{gap}}$  and then decreases as  $U^{-1}$  in the strong-coupling limit. This behaviour can be understood with a strong-coupling expansion in which the Cooper pairs are tightly bound and move in the lattice with an effective hopping  $J \sim t^2/U$ , with  $t$  the scale of the single-particle hopping<sup>15</sup>. The linear dependence of the critical temperature and of the superfluid weight with the interaction strength for  $U \lesssim E_{\text{gap}}$  is a robust result that has been verified using advanced many-body methods, such as dynamical mean-field theory<sup>14,15</sup>, quantum Monte Carlo<sup>48,49</sup> and density matrix renormalization group<sup>50–52</sup>. The dependence can be almost linear also in the presence of a band touching between the flat band and the other bands<sup>14</sup>.

### Superfluidity and topology in TBG

Remarkable interacting phases have been observed in TBG when the two layers are twisted with respect to each other by a ‘magic’ angle  $\theta \approx 1.1^\circ$  (FIG. 3a). These phases

include correlated (sometimes Chern) insulators at integer filling  $\nu$  of a set of eight flat bands (two per valley per spin quantum numbers) around charge neutrality, with superconductors for fillings in between<sup>2,3,45,53–99</sup> (FIG. 3b). Scanning tunnelling microscopy experiments reveal a Coulomb repulsion strength ( $\sim 25$  meV)<sup>61</sup> larger than the electron bandwidths. The strongly correlated insulators<sup>61</sup> at integer filling  $\nu \in [-4, 4]$  measured from charge neutrality acquire Chern numbers  $\pm(4 - |\nu|)$ <sup>59,63–66</sup>. Theoretically, the interacting TBG<sup>45,79–94,100,101</sup> is governed by<sup>79</sup> an approximate  $U(4)$  symmetry (later extended to  $U(4) \times U(4)$ ) (REFS<sup>72,93</sup>). The correlated insulator phases can be understood as ferromagnets of this large symmetry group<sup>79,80,93,102</sup>.

**TBG superconductivity.** Moiré materials host superconductivity<sup>3,55,57,103,104</sup> even at the — by far — lowest densities ever:  $10^{10}$ – $10^{12} \text{ cm}^{-2}$  (REFS<sup>103,104</sup>), which, for the sample sizes used, means 1,000–10,000 electrons. What causes

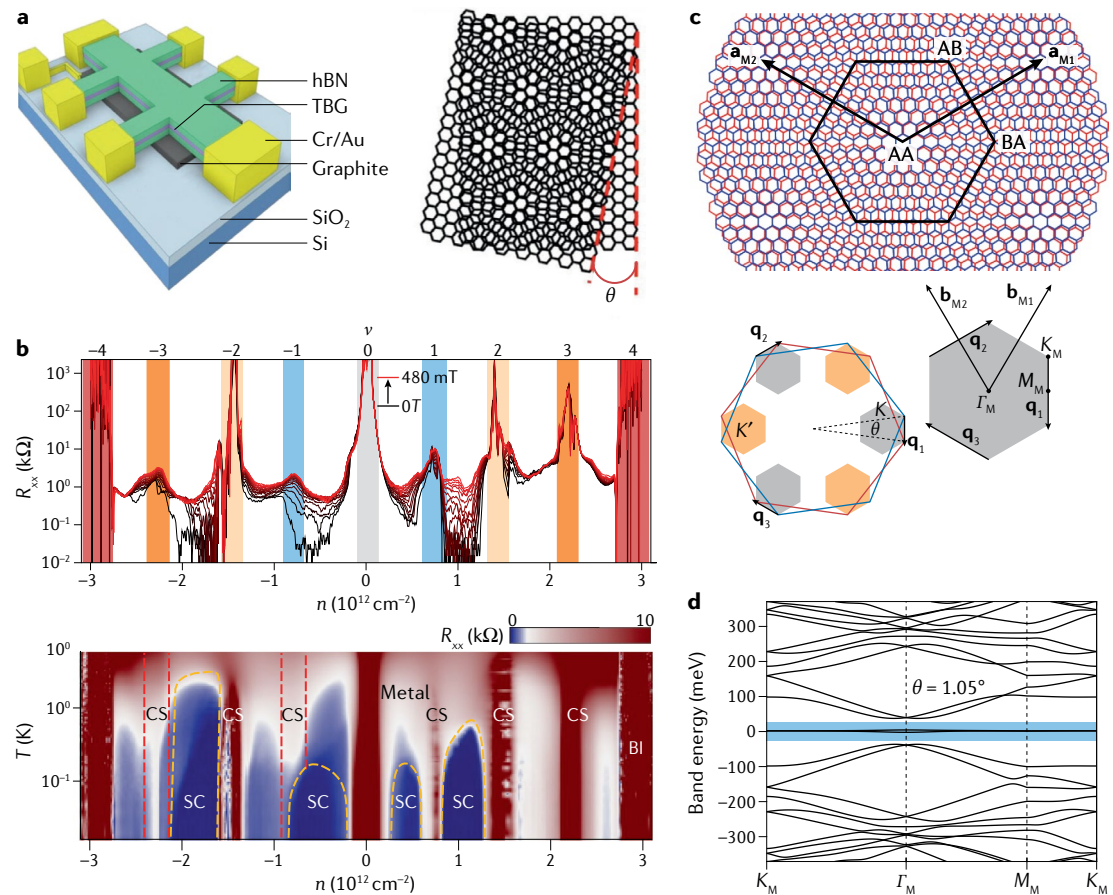


**Fig. 3 | Twisted bilayer graphene lattice, experimental phase diagram and band structures.** **a** | Sample for encapsulated moiré twisted bilayer graphene (TBG) lattice for a rotation angle  $\theta$ . **b** | Experimental observation of correlated insulators (CS, correlated states) — the red regions of the plots where the resistance ( $R_{xx}$ ) peaks — at integer fillings  $\nu$  of the two flat bands shaded in **d** and superconducting (SC) phases (low-resistance regions in blue) between the insulating phases and band insulators (BI). Here,  $T$  is the temperature and  $n$  is the density. **c** | Top, the moiré unit cell, where the blue sheet and the red sheet represent the top and bottom layers, respectively (top). In the AA, AB and BA regions, the A sublattice of the top layer is located above the A sublattice, the B sublattice and the hexagon centre of the bottom layer, respectively. Bottom left, the moiré Brillouin zone (BZ). The grey and orange hexagons represent the moiré BZ for the graphene valleys K and K', respectively. Bottom right, the reciprocal lattices and the high-symmetry momenta of the moiré BZ in graphene valley K. **d** | The band structure of the magic-angle  $\theta = 1.05^\circ$  TBG with its two flat bands (for one valley) using the Bistritzer–MacDonald model. hBN, hexagonal boron nitride. Panel **a** adapted from REF.<sup>99</sup>, under a Creative Commons licence CC BY-NC 4.0. Panel **b** adapted from REF.<sup>54</sup>, Springer Nature Ltd. Panels **c** and **d** adapted with permission from REF.<sup>97</sup>, APS.

superconductivity to appear at about 1–5 K in this most dilute of all known systems? Experimental evidence links superconductivity in TBG to the presence of flat bands at the magic angle. Away from these angles, superconductivity disappears. Regardless of the mechanism of TBG superconductivity, since the TBG flat bands exhibit zero total Chern number, is there a bound on their superfluid weight? What influence could the quantum geometry of the TBG bands have on the superfluid weight of TBG?

The moiré unit cell contains tens of thousands of atomic sites for small angles; such a large number of bands is impractical to handle in most calculations. Fortunately, many approximate approaches exist. At low energies, the single-particle TBG flat bands are well described by the Bistritzer–MacDonald model<sup>53</sup>. This model describes the coupling of the band structures of the top and bottom layers, which are rotated with respect to each other by  $\pm\theta/2$  around the  $z$ -axis. Each band structure separately consists of two Dirac points at the time-reversal ( $T$ ) partner momenta  $K$  and  $K'$  of the single-layer graphene Brillouin zone (FIG. 5c). When  $\theta$  is small such that the interlayer coupling is smooth in real space (with a length scale of variation much larger than the atom distances), the graphene valley ( $K$  and  $K'$ ) is a good quantum number of low-energy states of TBG<sup>53</sup> and, due to its conservation, the Dirac states around  $K$  ( $K'$ ) in the top layer only couple to the states around  $K$  ( $K'$ ) in the bottom layer. The Dirac Hamiltonian around  $K$  in the top layer is

$$\begin{aligned} h(\theta) = & -i\nu_F \partial_x \left( \cos \frac{\theta}{2} \sigma_x - \sin \frac{\theta}{2} \sigma_y \right) \\ & -i\nu_F \partial_y \left( \cos \frac{\theta}{2} \sigma_y + \sin \frac{\theta}{2} \sigma_x \right) \\ & \approx -i\nu_F \partial_r \cdot \sigma + i\frac{\theta}{2} \nu_F \partial_r \times \sigma, \end{aligned} \quad (18)$$

where  $\nu_F$  is the Fermi velocity of single-layer graphene and  $\sigma = (\sigma_x, \sigma_y)$  are Pauli matrices representing the A/B sublattices of graphene. For the bottom layer, we replace  $\theta \rightarrow -\theta$ . The interlayer coupling is encoded in a position-dependent matrix  $T(\mathbf{r})$ , such that the Hamiltonian of TBG, at valley  $K$ , can be written as

$$\begin{aligned} H(\mathbf{r}) = & -i\nu_F \tau_0 \partial_r \cdot \sigma - \frac{\theta}{2} \tau_z \partial_r \times \sigma \\ & + \begin{pmatrix} 0 & T(\mathbf{r}) \\ T^\dagger(\mathbf{r}) & 0 \end{pmatrix}. \end{aligned} \quad (19)$$

Here,  $\tau_0$  and  $\tau_z$  are the identity and the third Pauli matrices for the layer degree of freedom, respectively. Reference<sup>53</sup> derived  $T(\mathbf{r})$  for small  $\theta \sim 1^\circ$ :

$$T(\mathbf{r}) = \sum_{i=1}^3 e^{-i\mathbf{q}_i \cdot \mathbf{r}} T_i \quad (20)$$

where the  $\mathbf{q}_i$ s are  $\mathbf{q}_1 = k_D(0, -1)$ ,  $\mathbf{q}_2 = k_D(-\frac{\sqrt{3}}{2}, \frac{1}{2})$  and  $\mathbf{q}_3 = k_D(-\frac{\sqrt{3}}{2}, \frac{1}{2})$ , with  $k_D = 2|K|\sin\frac{\theta}{2}$  being the distance between  $K$  momenta in the two layers, and  $\nu_F = 5.944 \text{ eV}\text{\AA}$ ,  $|K| = 1.703 \text{ \AA}^{-1}$ . The  $T_i$ s are

$$T_i = w_0 \sigma_0 + w_1 \left[ \sigma_x \cos \frac{2\pi(i-1)}{3} + \sigma_y \sin \frac{2\pi(i-1)}{3} \right], \quad (21)$$

where the AA and AB hopping are  $w_1 = 110 \text{ meV}$  and  $w_0 = 0.7w_1$ , respectively. The translation symmetry of the moiré potential (Eq. (20)) under the moiré unit cell translations  $\mathbf{a}_{M1} = \frac{2\pi}{k_D}(-\frac{1}{\sqrt{3}}, \frac{1}{3})$  and  $\mathbf{a}_{M2} = \frac{2\pi}{k_D}(-\frac{1}{\sqrt{3}}, \frac{1}{3})$  is manifest in real space (FIG. 3c). At  $\theta \approx 1.1^\circ$ , there are two very flat bands (FIG. 3d, marked with blue); these are conventionally referred to as the ‘active bands’ of TBG.

**The BKT temperature and geometric contribution in TBG.** Being near the BKT transition is manifested in electron transport as  $V \propto I^3$  dependence between the longitudinal voltage  $V$  and the current  $I$ . Using this,  $T_{\text{BKT}}$  was estimated in REF.<sup>3</sup> to be about 1 K; however, the fit to  $I^3$  was partial. In a more recent work on magic-angle twisted trilayer graphene, a clear  $I^3$  behaviour was observed, giving  $T_{\text{BKT}} \approx 2.1 \text{ K}$  (REF.<sup>105</sup>).

Theoretically, the BKT temperature of TBG superconductors was estimated in REFS<sup>45,82,83</sup>; for a brief introduction, see REF.<sup>106</sup>. Reference<sup>83</sup> utilized the low-energy Bistritzer–MacDonald model described above and considered local  $s$ -wave pairing, leading to a local mean-field order parameter  $\Delta$ . Reference<sup>82</sup> presents a more microscopic approach, where the full tight-binding TBG Hamiltonian is reduced to a model that is manageable but still has a large unit cell of a few hundreds of atoms, by using the so-called renormalization moiré method<sup>107,108</sup>. A low-energy continuum calculation was presented as a comparison with the renormalization moiré calculations. Both local  $s$ -wave and nearest-neighbour resonance valence bond pairing were considered. In the latter, the order parameter  $\Delta$  corresponds to pairing of electrons in neighbouring sites. Works in REFS<sup>82,83</sup> both found that  $T_{\text{BKT}}$  at the magic angle is influenced by the geometric contribution of superconductivity (Eq. (12)). In REF.<sup>83</sup>, it was shown that the geometric contribution to the superfluid weight is about twice as large as the conventional one at the magic angle, while slightly away from the magic angle, the conventional one starts to dominate (FIG. 4a,b). As the pairing mechanism and the interaction strength in TBG are not precisely known at the moment, no accurate predictions of  $T_{\text{BKT}}$  could be made in REFS<sup>45,82,83</sup>; however, the estimates gave temperatures in the few Kelvin range, consistent with the experiments. Assuming  $\Delta(T) \approx 2k_B T_c^*(1 - T/T_c^*)^{1/2}$  (REF.<sup>26</sup>), the ratio between the Cooper pair formation (BCS) critical temperature  $T_c^*$  and  $T_{\text{BKT}}$  was found for the filling ratio  $\nu = 1/4$  (two electrons per moiré unit cell) to be  $T_{\text{BKT}}/T_c^* = 0.35$  (REF.<sup>45</sup>). For the geometric contribution of the TBG superfluid weight  $D_s$  at zero temperature, using the experimental  $T_{\text{BKT}} = 1.5 \text{ K}$  (REF.<sup>3</sup>) and an order parameter  $\Delta = 2k_B T_c^* \approx 0.74 \text{ meV}$ , the value  $[D_s]_{\text{geom}} \approx \frac{4e^2\Delta}{\pi\hbar^2} \sqrt{\nu(1-\nu)} \approx 1.5 \times 10^8 \text{ H}^{-1}$  was obtained<sup>45,82,83</sup>. This is one order of magnitude smaller than the superfluid weight in BSCCO and MoGe, but for a TBG density two orders of magnitude smaller ( $n \approx 10^{12} \text{ cm}^{-2}$ ).

TBG superconductivity is often described by models featuring only the four nearly flat bands, as it is assumed that the low-energy physics dominates. Importantly, however, the work in REF.<sup>82</sup> suggests that neglecting

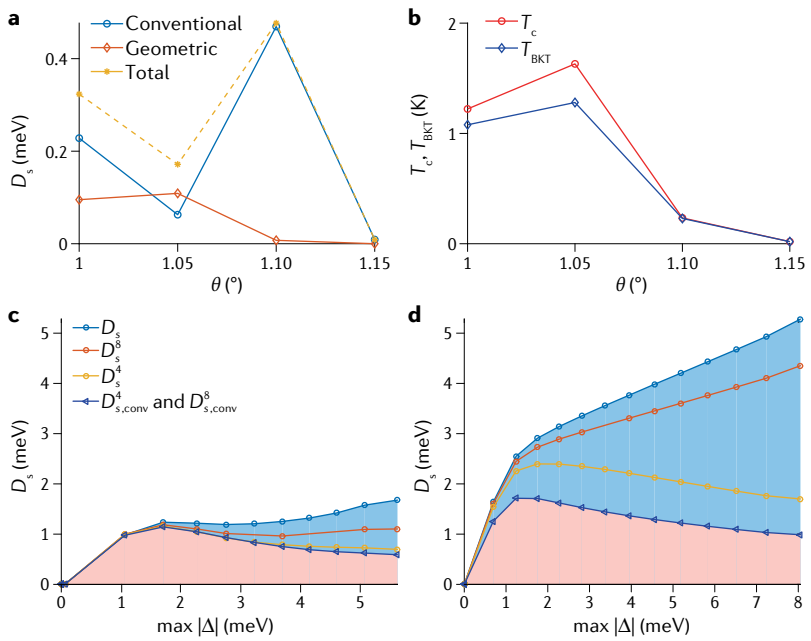


**Fig. 4 | Geometric contribution in twisted bilayer graphene superfluid weight.**

**a** | Superfluid weight  $D_s$  as a function of the twist angle  $\theta$ . The geometric contribution of  $D_s$  is larger than the conventional one at the magic angle  $1.05^\circ$ , while away from it, the conventional one dominates. **b** | Critical temperature,  $T_c$  as a function of  $\theta$ , which changes from Berezinskii–Kosterlitz–Thouless (BKT) type ( $T_{BKT}$ ) to the conventional Bardeen–Cooper–Schrieffer one ( $T_c$ ) when moving away from the magic angle. **c,d** | Superfluid weight as a function of the order parameter (as it is spatially varying, the maximum  $|\Delta|$  is used). The order parameter is varied by changing the coupling constant of the interaction term, which is a nearest neighbour (resonance valence bond) interaction in **c** and a local interaction in **d**. Here,  $D_s^4$  and  $D_s^8$  (and  $D_s^4$  and  $D_s^8$  conv) are the total (only conventional part of) superfluid weights calculated including only the four nearly flat bands or the eight lowest (four flat, four dispersive) bands, respectively, and  $D_s$  is the converged result including 40 of the 676 bands of the renormalization moiré model. For interactions that are large compared with the bandwidth, the flat-band limit is reached and the geometric contribution (blue area) becomes larger than the conventional one (pink). The lines marked with different symbols show that the conventional contribution is captured well by including only the four lowest bands in the calculation, while more than eight are needed to obtain the correct result in the case of the geometric contribution that arises from interband processes. Panels **a** and **b** adapted with permission from REF.<sup>83</sup>, APS. Panels **c** and **d** adapted with permission from REF.<sup>82</sup>, APS.

higher bands may not be adequate when calculating the BKT temperature; the underlying reason is that the geometric contribution of the superfluid weight is due to interband processes that do not scale as one over the band gap, as one might naively expect for processes involving higher bands (see Eqs (12) and (13) and REF.<sup>15</sup>). The TBG superfluid weight divides into the conventional and geometric contributions, the latter becoming dominant when interactions exceed the bandwidth, that is, the flat-band regime is approached (FIG. 4c,d), indicating that considerably more than four bands need to be included to obtain quantitatively or even qualitatively correct results. In choosing effective low-energy models with only a few bands, one should, thus, pay attention to the quantum geometric properties of its Bloch functions, in addition to the dispersion and symmetries. One more finding in REF.<sup>82</sup> was that, in the case of the resonance valence bond pairing, the superfluid is nematic and the corresponding superfluid weight is anisotropic, thus measurements of the superfluid weight could distinguish

between local or non-local pairing mechanism through (an)isotropy.

The linear dependence of the BKT temperature on interaction in the case of TBG was confirmed by Monte Carlo calculations<sup>49</sup>. The same was found to hold for the temperatures where the single-particle density of states and the spin susceptibility reach their maxima. These temperatures were higher than the BKT temperature, indicating singlet and gap formation already above the temperature for superconductivity. Such pseudogap formation was also studied in REF.<sup>109</sup> for a flat-band model different from TBG. It was pointed out that the ratio between the pseudogap temperature and  $T_{BKT}$  can inform about the geometric contribution of the preformed pair effective mass.

Besides moiré materials, the geometric contribution to the superfluid weight has been found to be important in another 2D superconductor, monolayer FeSe grown on a SrTiO<sub>3</sub> (STO) substrate<sup>110</sup>, which has a critical temperature of 65 K. FeSe on STO has a large ratio  $T_c/T_F \sim 0.1$  between critical temperature and Fermi temperature, even larger than that of TBG<sup>3</sup> (a property shared with its parent compound: bulk FeSe (REF.<sup>111</sup>)). These findings validate the general picture that the effect of quantum geometry on superfluidity is crucial in materials close to the flat-band limit.

**Fragile and stable topology.** The TBG eigenstates exhibit subtle topology of either a fragile or stable type, depending on the symmetries kept in the model. The single-graphene-valley Hamiltonian (Eq. (19)) has the symmetries of the magnetic space group  $P6'2'2$  (REF.<sup>73</sup>) (#177.151 in the BNS setting<sup>112</sup>): (i)  $C_{2z}T = \sigma_zK$ , where  $K$  is the complex conjugation, (ii)  $C_{3z} = e^{i\frac{2\pi}{3}\sigma_z}$  and (iii)  $C_{2x} = \tau_x\sigma_x$ . The  $C_{2z}$  rotation and the time-reversal  $T$  separately are not symmetries of Eq. (19), since they map the graphene valley  $K$  into  $K'$ . An important, non-crystalline symmetry for a small twist angle is a unitary particle-hole inversion operation  $P = i\tau_y$ , for which  $PH(\mathbf{r})P^\dagger = -H(-\mathbf{r})$ . Crucially, it has been proved that these symmetries force the single-valley TBG model to be topological at any small twist angle and that the active bands of TBG cannot be described by localized symmetric Wannier states<sup>73</sup>. To explain that, recall that the Wannier functions  $w_\alpha(\mathbf{i}, \alpha)$  (Eq. (16)) are spread in space ( $\mathbf{i}$  and  $\alpha$  are the unit cell and orbital indices, respectively). One can define the ‘centre’ of the Wannier function as the average location, measured from the origin; scaled by the unit length, this corresponds to the Berry phase<sup>19,113</sup>. When Fourier transforming (Eq. (16)) with  $k_y$  only, the Wannier centre in the  $y$  direction will depend on  $k_x$ . This motion of the Wannier centre as a function of the Brillouin zone momentum  $k_x \in [0, 2\pi]$  is called the Wilson loop<sup>19,113</sup> and is shown for TBG in FIG. 5a. Importantly, it winds between  $\pi$  and  $-\pi$ . This means that the Wannier functions cannot be simultaneously localized in  $x$  and  $y$ : such localization would imply that the  $y$  Wannier centre cannot move across the entire  $y$ -unit cell as  $k_x$  is varied across the Brillouin zone.

The type of topology that the valley-filtered bands respect has been subject to revision. In the initial

papers<sup>69,72–74,114,115</sup>, the topology was thought to be of a new, fragile type<sup>76,116,117</sup> protected by  $C_{2z}T$  (this type of topology does not require any of the other symmetries of TBG). Fragile topology is an obstruction to constructing symmetric Wannier functions for a given set of bands, which can be removed by adding other topologically trivial bands to the Hilbert space<sup>116,117</sup>. Computing the Wilson loop of more than the two bands around charge neutrality (FIG. 5a) causes crossings at different Wilson eigenvalues (FIG. 5b) at any small coupling. Consequently, the Wannier centre winding disappears, the band topology is trivialized and one can construct localized Wannier functions. Very recently, it was realized<sup>97</sup> that, if one further imposes the particle–hole symmetry  $P$  on TBG, the topology becomes stable and not fragile. The combined antiunitary operator  $(PC_{2z}T)^2 = -1$  mimics the case of spinful time-reversal symmetry and protects Kramers doublets in the Wilson spectrum at  $k_{M1} = 0$  and  $k_{M1} = \pi$  (REFS<sup>113,118</sup>) (FIG. 5d). The flow of the Wannier centres in TBG thus shows winding (FIG. 5c,d) and the valley- $K$  model (Eq. (19)) is always strongly topological, no matter how many bands are included. Mixing the other valley renders the topology trivial; at small angles, however, the two valleys do not mix<sup>53</sup>.

**Lower bound of superconductivity in TBG from topology.** The winding of the Wilson loop reflecting the topology of the active bands in TBG<sup>73</sup> can also be characterized by an integer-valued invariant, Euler or

Stiefel–Whitney class,  $e_2 = 1$  (REF.<sup>75</sup>). References<sup>73,75,97</sup> showed that this implies the existence of  $4l + 2e_2$  ( $l$  an integer) Dirac nodes at zero energy between the two active bands that cannot be energetically separated. As mentioned earlier, the superfluid weight of topological bands should be non-zero; however, the inequality bound Eq. (17) cannot be used, as the Chern number is zero due to the  $C_{2z}T$  symmetry. Instead, the symmetry class of  $(C_{2z}T)^2 = 1$  provides a new lower bound for the superfluid weight in TBG<sup>45</sup>, using the universally true Eq. (15). The non-Abelian Berry connection and curvature of the two TBG flat bands can be written as in BOX 1, under a proper local gauge choice on a patch in the Brillouin zone<sup>59,73,74,114</sup>. In REF.<sup>45</sup>, it was proved that the Wilson loop winding number in REF.<sup>73</sup> is equivalent to the Euler class  $e_2$  in REF.<sup>114</sup>, whose expression is given in BOX 1 (Eq. (27)).

Using the positive definiteness of the non-Abelian QGT  $\mathfrak{G}_{ij}$ , it was shown<sup>45</sup> that the quantum metric is bounded by the off-diagonal part  $f_{xy}$  of the non-Abelian Berry curvature  $\mathcal{F}_{xy} : \text{tr } g \geq 2|f_{xy}|$ , which, in turn, means that the superfluid weight is bounded by the Euler characteristic:

$$\frac{1}{4\pi} \int_{BZ} d^2k \text{tr } g(\mathbf{k}) \geq \frac{1}{2\pi} \int_{BZ'} d^2k |f_{xy}| \\ \geq \left| \frac{1}{2\pi} \int_{BZ'} d^2k f_{xy} \right| = |e_2|.$$

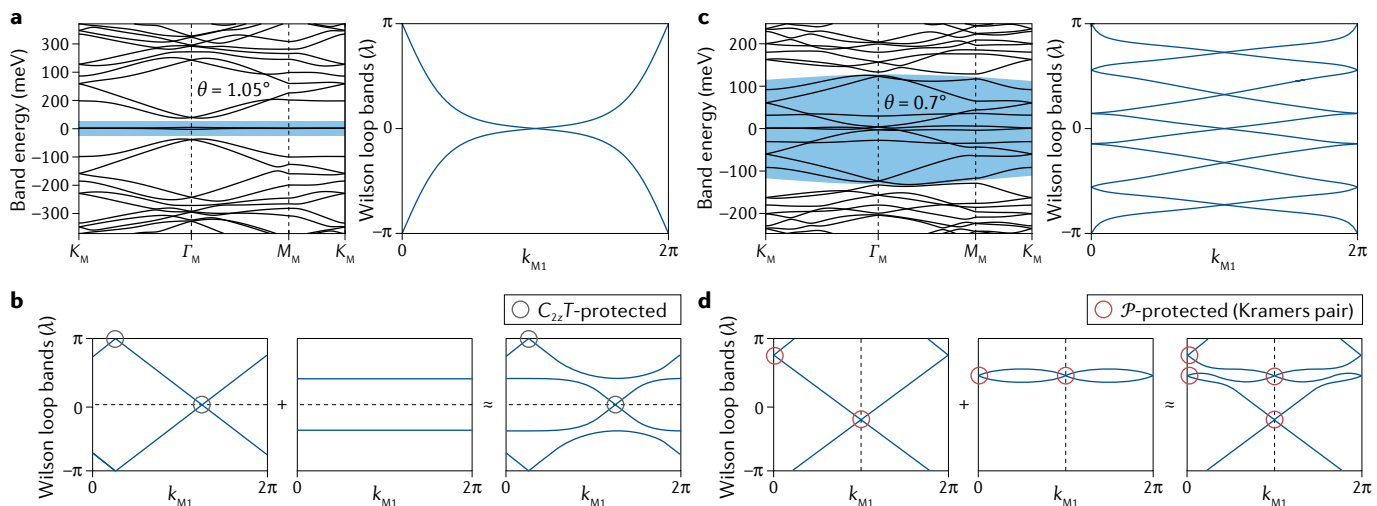


**Fig. 5 | Wilson loops/Wannier centres: fragile and stable topology of twisted bilayer graphene.** **a** Left, the band structure of the magic-angle  $\theta = 1.05^\circ$  twisted bilayer graphene with its two flat bands (using the Bistritzer–MacDonald model, single valley). Right, their hybrid Wannier centres — the Wilson loop bands. The crossings in the Wilson loop bands are protected by  $C_{2z}T$  and/or by particle–hole  $P$ ; the double degeneracies with  $\lambda \neq 0, \pi$  at  $k_1 = 0, \pi$  are protected by the approximate  $\mathcal{P}$  symmetry. These double degeneracies guarantee winding of the Wilson loops across the Brillouin zone for any bands with  $4n+2$  Dirac nodes at zero energy. The parameters of the Hamiltonian used in **a–d** are  $v_F = 5.944 \text{ eV}\text{\AA}$ ,  $|\mathbf{K}| = 1.703 \text{ \AA}^{-1}$ ,  $w_1 = 110 \text{ meV}$  and  $w_0 = 0.7w_1$ . **d** Comparison of Wilson loop windings protected by  $\mathcal{P}$  and  $C_{2z}T$ . The crossings at  $k_{M1} = 0, \pi$  are Kramers pairs protected by  $\mathcal{P}$ . The  $Z_2$  Euler invariant equals 1 if the Wilson loop bands form a zigzag connection between  $k_{M1} = 0$  and  $k_{M1} = \pi$ , and equals 0 otherwise. The  $\mathcal{P}$ -protected topology is stable against adding trivial bands: coupling the non-trivial Wilson loop bands (left) to trivial Wilson loop bands (middle) yields non-trivial Wilson loop bands (right). Panels **a–d** adapted with permission from REF.<sup>97</sup>, APS.

(right) of the middle ten bands of twisted bilayer graphene (shaded) at  $\theta = 0.7^\circ$ . The crossings at the Wilson eigenvalue  $\lambda = 0, \pi$  in the Wilson loop bands are protected by  $C_{2z}T$  and/or by particle–hole  $P$ ; the double degeneracies with  $\lambda \neq 0, \pi$  at  $k_1 = 0, \pi$  are protected by the approximate  $\mathcal{P}$  symmetry. These double degeneracies guarantee winding of the Wilson loops across the Brillouin zone for any bands with  $4n+2$  Dirac nodes at zero energy. The parameters of the Hamiltonian used in **a–d** are  $v_F = 5.944 \text{ eV}\text{\AA}$ ,  $|\mathbf{K}| = 1.703 \text{ \AA}^{-1}$ ,  $w_1 = 110 \text{ meV}$  and  $w_0 = 0.7w_1$ . **d** Comparison of Wilson loop windings protected by  $\mathcal{P}$  and  $C_{2z}T$ . The crossings at  $k_{M1} = 0, \pi$  are Kramers pairs protected by  $\mathcal{P}$ . The  $Z_2$  Euler invariant equals 1 if the Wilson loop bands form a zigzag connection between  $k_{M1} = 0$  and  $k_{M1} = \pi$ , and equals 0 otherwise. The  $\mathcal{P}$ -protected topology is stable against adding trivial bands: coupling the non-trivial Wilson loop bands (left) to trivial Wilson loop bands (middle) yields non-trivial Wilson loop bands (right). Panels **a–d** adapted with permission from REF.<sup>97</sup>, APS.

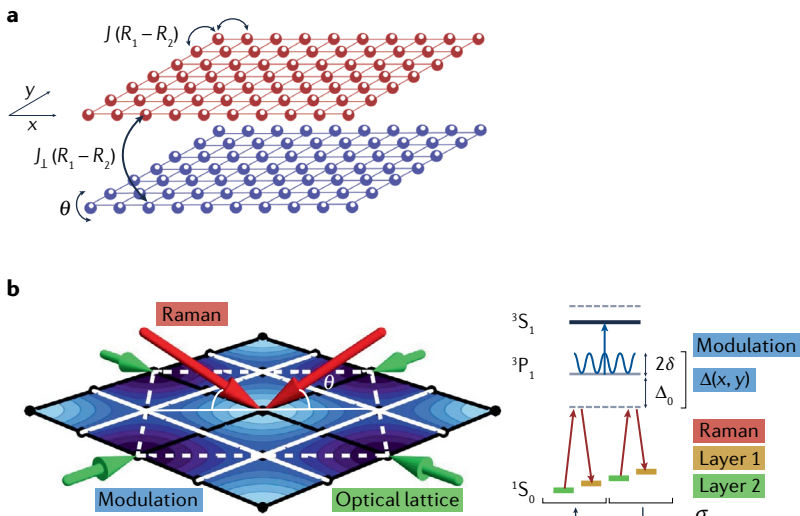


**Fig. 6 | Ultracold gas analogues of twisted bilayer graphene.** **a** | Two square optical lattices (red and blue) with an angle  $\theta$  between them form the analogue of the two layers in twisted bilayer graphene. The two optical lattices are displaced in the z direction for clarity. In reality, they would be spatially overlapping and trap separately two long-lived atomic states, which play the role of the layer degree of freedom. There is no interference pattern between the two optical lattices, since the corresponding light fields have orthogonal polarizations. The intralayer hopping  $J$  is tuned by adjusting the depth of the two optical lattices, while a tunable interlayer hopping  $J_{\perp}$  can be generated using either a direct transition, using microwave radiation, or an indirect Raman transition between the atomic states. Schematic of the proposal of REF.<sup>136</sup>. **b** | A single state-insensitive optical lattice (green) with spatially dependent Raman coupling. This is obtained with a spatially varying detuning  $\Delta(x, y)$  of the Raman beams induced by a ‘modulation laser’ (blue). This has the effect of modulating the interlayer hopping  $J_{\perp}$  in a way similar to the spatial twisting of the optical lattices in panel **a**. Panel **a** adapted with permission from REF.<sup>136</sup>, APS. Panel **b** adapted with permission from REF.<sup>137</sup>, APS.

**Quantum geometry in the correlated insulator states of TBG.** Remarkably, a generalization of the quantum metric also appears in the TBG correlated insulator states<sup>98</sup>. Being in the strong coupling limit, TBG interacting states of matter<sup>45,79–94</sup> depend chiefly on the eigenstates (but not the energies) of the flat bands. The insulating states in TBG at integer filling are amongst the best studied experimentally and theoretically, and the least theoretically controversial, as extensive theoretical efforts have been aimed at their explanation<sup>79–81,84–94</sup>.

The strong coupling TBG Coulomb Hamiltonians<sup>69,79,102,119,120</sup> (similar to the negative  $U$  projected Hubbard models in the superfluid weight) allow for exact expressions of energy and eigenstate of the charge  $\pm 1$  excitation (relevant for transport gaps), of neutral excitation and of charge  $\pm 2$  excitation (relevant for possible Cooper pair binding energy). The charge 1 excitation dispersion is governed by a generalized QGT of the projected bands, convoluted with the Coulomb interaction<sup>93,102</sup>. Hence, the QGT influences the charge excitation dispersion of the insulating states of TBG, similar to how it governs the Cooper pair dispersion for the attractive Hubbard model. Hence, it seems that, whether superconductivity develops out of the topological bare flat bands or if it develops upon doping the dispersive excitation of the insulating state, the QGT plays a crucial role in both scenarios: it either gives non-zero superfluid weight or creates large quasiparticle dispersion, respectively.

## Multilayers and flat bands in ultracold gases

Atoms trapped by magnetic fields and light-induced potentials can be cooled to extremely low temperature and, by means of laser standing waves, it is possible to force the atoms to move on the discrete lattice formed by the local minima of the optical potential, thereby mimicking the lattice of atomic orbitals in solids<sup>121–125</sup>. These optical lattices are just one example of the high degree of tunability of ultracold gases, which makes them an excellent quantum simulation platform to tackle currently intractable problems in quantum many-body physics and condensed matter physics. After the realization of Bose–Einstein condensates and quantum degenerate Fermi gases, experiments with ultracold gases have become increasingly sophisticated. The rich and versatile ultracold gas experimental toolbox has allowed to realize, among other things, artificial graphene lattices<sup>126,127</sup>, geometries displaying flat bands like kagome<sup>128</sup> and Lieb<sup>129</sup> lattices, bilayers<sup>130</sup>, quasicrystals<sup>131</sup> and synthetic dimensions<sup>132–134</sup>. Moiré patterns have been predicted to occur also in vortex lattices in Bose–Einstein condensates<sup>135</sup>.

The phase diagram of TBG depending on the twist angle and filling is currently a hotly debated subject, and proposals have been put forward recently for realizing an ultracold gas analogue of TBG<sup>136–139</sup> and investigating this problem in a well-controlled setting. The central idea common to all proposals is to use the internal hyperfine states of the atoms to encode the layer degree of freedom of TBG as a synthetic dimension. The proposals of REFS<sup>136,139</sup> rely on an optical potential, which depends on the hyperfine state. In this way, it is possible to realize optical lattices for different atomic states that are twisted with respect to each other (FIG. 6a). There are different methods to realize a state-dependent optical potential, but they all rely on a clever arrangement of the laser field polarizations and the level structure of the atoms. The interlayer tunnelling is engineered either by coupling the two states directly with microwave radiation or by a two-photon Raman transition. Alternatively, it is possible to obtain the same result by using a single state-insensitive optical lattice together with a spatially modulated Raman coupling<sup>137</sup> (FIG. 6b). In the latter case, the period of the moiré pattern is precisely the period of the modulation of the Raman detuning and one can avoid to physically twist the optical lattices.

The first strategy of tilted state-dependent optical lattices has been used in a recent experimental implementation with rubidium-87 (REF.<sup>140</sup>). Whereas <sup>87</sup>Rb is bosonic, a generalization of the same scheme for fermionic atoms could allow to realize a faithful model of TBG in the near future. These recent results demonstrate that twisted bilayers are feasible within the ultracold gas toolbox. However, to probe the effect of quantum geometry on superfluidity, it is also necessary to measure observables such as the superfluid weight, in particular, its dependence on the interaction strength.

A whole set of new ideas and methods are required for measuring such observables in ultracold gases<sup>141</sup>. A lot of work has already been done in this direction: in the case of the unitary Fermi gas, the superfluid fraction has been measured by directly imaging the density variations associated to the propagation of a wave of

second sound<sup>142</sup>, a mode characterized by out-of-phase oscillations of the normal and superfluid components.

Some theoretical ideas for measuring the superfluid density are a direct analogue of the classical experiment with helium II by Andronikashvili: a finite angular velocity is imparted to the ultracold gas, either by rotating the optical trap or by using a light-induced vector potential, and then the moment of inertia, directly related to the superfluid fraction, is obtained from the density redistribution<sup>143</sup> or spectroscopically from the hyperfine level population<sup>144,145</sup>. Other approaches based on artificial gauge fields can allow the measurement of the superfluid density at a local level and out of equilibrium<sup>141</sup>. The ability to bring the ultracold gas out of equilibrium by suddenly changing a control parameter (called a quench) can also be useful to measure the superfluid weight in lattice systems<sup>146,147</sup>. Another route to investigate the transport properties in a rather direct fashion is to realize two-terminal setups with ultracold gases<sup>148,149</sup>, such as the one that has allowed to observe superfluid flow in the presence of disorder<sup>150</sup>. In a two-terminal setup, superfluid transport can be investigated also through the Josephson effect<sup>151</sup>.

### Outlook

The fingerprint of quantum geometric flat-band superconductivity is the linear dependence on the (weak) interaction of the following quantities: Cooper pairing temperature, the pairing gap, superfluid weight and the BKT superfluid transition temperature — the linear dependence holds when the interaction is smaller than or similar to the hopping energies. Experiments where (at least some of) these quantities are measured while varying the interaction would reveal — if approximately linear dependence is seen — the geometric contribution of superfluidity for the first time. The normal state above the critical temperature is also likely to reveal interesting preformed pair, pseudogap or insulator behaviour characteristic for a flat band<sup>49,50,60,109,152</sup>.

As platforms, the 2D moiré materials<sup>4–8</sup> and ultracold gases<sup>121–124</sup> are complementary. Although a remarkable demonstration on tuning the electronic interactions via an electric field exists in twisted graphene<sup>105</sup>, in general, the control of interaction is easier and more precise in ultracold gases. There, the Feshbach resonance technique<sup>153</sup> allows realizing negative or positive interaction strengths of any magnitude, without affecting any other system parameter. The microscopic interaction is well approximated by a contact interaction, allowing to test Hubbard-type theories precisely. Another advantage of ultracold gas setups is that the ratio between interlayer and intralayer tunnelling amplitudes can be adjusted more freely than in moiré materials. This opens up the possibility of observing quasi-flat bands for larger rotation angles (smaller moiré unit cells) for instance. The great advantage of the 2D materials is that the temperatures required for superconductivity can actually be reached. While continuum ultracold gases routinely show superfluidity, bringing fermions in lattices to the superfluid temperatures is a challenge, although advances in realizing antiferromagnetic states<sup>154</sup> suggest that it should be reached soon. In the

meantime, ultracold gases are suitable for exploring the normal state and bosonic superfluidity. Ultracold gases are clean systems where impurities can be added in a controllable way, so they are an excellent platform for understanding the effect of disorder. The quantum gas microscopes<sup>123</sup> provide direct information about the fluctuations and quantum correlations of the ground state. For TBG, revealing quantum geometry effects via noise measurements has been proposed<sup>155</sup>. The charge quasiparticle dispersion, which is related to the QGT, can be revealed by scanning tunnelling microscopy. Concerning transport experiments, 2D materials are clearly the advantageous platform, although opportunities exist also in ultracold gases<sup>149,151</sup>. For TBG, experimental work exploring the role of quantum geometry in superconductivity has already started<sup>156</sup>.

Superconductivity in TBG is obviously only the beginning. Another promising moiré material is WTe<sub>2</sub>, where a topological exciton insulator has been observed in a single layer<sup>157</sup> but where metallic behaviour is obtained in moiré bilayers<sup>158</sup>; the appearance of superconductivity at some twist angles in WTe<sub>2</sub> would be interesting due to its topological bands. Transition to the superconducting state has been observed already in magic-angle twisted trilayer graphene<sup>105</sup>. Remarkably, the transition temperature in magic-angle twisted trilayer graphene was more than 2 K, larger than that in magic-angle TBG. Would stacking more layers eventually lead to room-temperature superconductivity, in the spirit of the early proposal<sup>9</sup>? Certainly, materials that have been thought to be non-superconducting in the past, such as untwisted graphene, become superconducting when three layers are stacked together<sup>159</sup>. Defining the highest possible critical temperature is an important research topic; recent works suggest the existence<sup>44,160</sup> or absence<sup>161</sup> of an upper bound. Due to the fundamental lower bound of superfluidity (Eqs (15) and (17)), one can expect higher critical temperatures for a large quantum metric or Chern number. However, these results assume the isolated flat-band limit; the quantum metric typically diverges when bringing other bands close to the flat band. While the divergence does not show up in the superfluid weight (due to the contribution of other bands), it still leads, in general, to the enhancement of the latter<sup>14</sup>. This hints to a possible sweet spot where quantum geometry effects are maximized by bringing other bands close to the flat band, while keeping them far enough away so that most of the pairing takes place in the flat band, where interactions dominate.

The quantum metric is a fundamental quantity describing distances between the eigenstates of a system and, hence, appears in many observables of interacting systems. For instance, light-matter interactions<sup>162,163</sup> and exciton condensates<sup>164</sup> in moiré materials reflect the underlying quantum geometry as well. Recently, quantum geometry was predicted to stabilize Bose-Einstein condensates in flat bands<sup>165</sup>, relevant for bosonic condensates in ultracold gas and polariton systems, or even for 2D moiré materials at the bosonic end of the BCS to Bose-Einstein condensation crossover<sup>105</sup>.

Published online 10 June 2022

1. Zhou, X. et al. High-temperature superconductivity. *Nat. Rev. Phys.* **3**, 462–465 (2021).
2. Cao, Y. et al. Correlated insulator behaviour at half-filling in magic-angle graphene superlattices. *Nature* **556**, 80–84 (2018).
3. Cao, Y. et al. Unconventional superconductivity in magic-angle graphene superlattices. *Nature* **556**, 43–50 (2018).
4. MacDonald, A. H. Bilayer graphene's wicked, twisted road. *Physics* **12**, 12 (2019).
5. Andrei, E. Y. & MacDonald, A. H. Graphene bilayers with a twist. *Nat. Mater.* **19**, 1265–1275 (2020).
6. Balents, L., Dean, C. R., Efetov, D. K. & Young, A. F. Superconductivity and strong correlations in moiré flat bands. *Nat. Phys.* **16**, 725–733 (2020).
7. Kennes, D. M. et al. Moiré heterostructures as a condensed-matter quantum simulator. *Nat. Phys.* **17**, 155–163 (2021).
8. Andrei, E. Y. et al. The marvels of moiré materials. *Nat. Rev. Mater.* **6**, 201–206 (2021).
9. Kopnin, N., Heikkilä, T. & Volovik, G. High-temperature surface superconductivity in topological flat-band systems. *Phys. Rev. B* **83**, 220503 (2011).
10. Heikkilä, T., Kopnin, N. & Volovik, G. Flat bands in topological media. *JETP Lett.* **94**, 233 (2011).
11. Khodel, V. A. & Shaginyan, V. R. New approach in the microscopic Fermi systems theory. *Phys. Rep.* **249**, 1–134 (1994).
12. Schrieffer, J. R. *Theory of Superconductivity. Frontiers in Physics* (Benjamin, 1964).
13. Peotta, S. & Törmä, P. Superfluidity in topologically nontrivial flat bands. *Nat. Commun.* **6**, 8944 (2015).
14. Julku, A., Peotta, S., Vanhala, T. I., Kim, D.-H. & Törmä, P. Geometric origin of superfluidity in the Lieb lattice flat band. *Phys. Rev. Lett.* **117**, 045303 (2016).
15. Liang, L. et al. Band geometry, Berry curvature and superfluid weight. *Phys. Rev. B* **95**, 024515 (2017).
16. Törmä, P., Liang, L. & Peotta, S. Quantum metric and effective mass of a two-body bound state in a flat band. *Phys. Rev. B* **98**, 220511 (2018).
17. Huhtinen, K.-E., Herzog-Arbeitman, J., Chew, A., Bernevig, B. A. & Törmä, P. Revisiting flat band superconductivity: dependence on minimal quantum metric and band touchings. Preprint at *arXiv* 2203.11133 (2022).
18. Provost, J. P. & Vallee, G. Riemannian structure on manifolds of quantum states. *Commun. Math. Phys.* **76**, 289–301 (1980).
19. Resta, R. The insulating state of matter: a geometrical theory. *Eur. Phys. J. B* **79**, 121–137 (2011).
20. Hasan, M. Z. & Kane, C. L. Colloquium: Topological insulators. *Rev. Mod. Phys.* **82**, 3045–3067 (2010).
21. Bernevig, B. A. & Hughes, T. L. *Topological Insulators and Topological Superconductors* (Princeton Univ. Press, 2013).
22. Mielke, A. Ferromagnetic ground states for the Hubbard model on line graphs. *J. Phys. A Math. Gen.* **24**, 2 (1991).
23. Lieb, E. H. Two theorems on the Hubbard model. *Phys. Rev. Lett.* **62**, 1201 (1989).
24. Leykam, D., Andreanov, A. & Flach, S. Artificial flat band systems: from lattice models to experiments. *Adv. Phys. X* **3**, 1473052 (2018).
25. Calugáru, D. et al. General construction and topological classification of crystalline flat bands. *Nat. Phys.* **18**, 185–189 (2022).
26. Tinkham, M. *Introduction to Superconductivity* 2nd edn (Dover Publications, 2004).
27. Scalapino, D., White, S. R. & Zhang, S. C. Superfluid density and the Drude weight of the Hubbard model. *Phys. Rev. Lett.* **68**, 2830 (1992).
28. Scalapino, D., White, S. R. & Zhang, S. C. Insulator, metal, or superconductor: The criteria. *Phys. Rev. B* **47**, 7995 (1993).
29. Chandrasekhar, B. S. & Einzel, D. The superconducting penetration depth from the semiclassical model. *Ann. Phys.* **505**, 535–546 (1993).
30. Leggett, A. J. On the superfluid fraction of an arbitrary many-body system at  $T=0$ . *J. Stat. Phys.* **93**, 927–941 (1998).
31. London, F. & London, H. The electromagnetic equations of the superconductor. *Proc. R. Soc. A Math. Phys. Eng. Sci.* **149**, 71–88 (1935).
32. Basov, D. N. & Chubukov, A. V. Manifesto for a higher  $T_c$ . *Nat. Phys.* **7**, 272–276 (2011).
33. Tovmasyan, M., Peotta, S., Törmä, P. & Huber, S. D. Effective theory and emergent SU(2) symmetry in the flat bands of attractive Hubbard models. *Phys. Rev. B* **94**, 245149 (2016).
34. Rossi, E. Quantum metric and correlated states in two-dimensional systems. *Curr. Opin. Solid State Mater. Sci.* **25**, 100952 (2021).
35. Iskin, M. Two-body problem in a multiband lattice and the role of quantum geometry. *Phys. Rev. A* **103**, 053311 (2021).
36. Oh, M. et al. Evidence for unconventional superconductivity in twisted bilayer graphene. *Nature* **600**, 240–245 (2021).
37. Moon, K. et al. Spontaneous interlayer coherence in double-layer quantum Hall systems: Charged vortices and Kosterlitz-Thouless phase transitions. *Phys. Rev. B* **51**, 5138–5170 (1995).
38. Kopnin, N. B. Surface superconductivity in multilayered rhombohedral graphene: Supercurrent. *JETP Lett.* **94**, 81 (2011).
39. Marzari, N., Mostofi, A. A., Yates, J. R., Souza, I. & Vanderbilt, D. Maximally localized Wannier functions: Theory and applications. *Rev. Mod. Phys.* **84**, 1419 (2012).
40. Chiu, C.-K., Teo, J. C. Y., Schnyder, A. P. & Ryu, S. Classification of topological quantum matter with symmetries. *Rev. Mod. Phys.* **88**, 035005 (2016).
41. Brouder, C., Panati, G., Calandra, M., Mourougane, C. & Marzari, N. Exponential localization of Wannier functions in insulators. *Phys. Rev. Lett.* **98**, 046402 (2007).
42. Panati, G. Triviality of Bloch and Bloch–Dirac bundles. *Ann. Henri Poincaré* **8**, 995–1011 (2007).
43. Monaco, D., Panati, G., Pisante, A. & Teufel, S. Optimal decay of Wannier functions in Chern and quantum Hall insulators. *Commun. Math. Phys.* **359**, 61–100 (2018).
44. Verma, N., Hazra, T. & Randeria, M. Optical spectral weight, phase stiffness, and  $T_c$  bounds for trivial and topological flat band superconductors. *Proc. Natl. Acad. Sci. USA* **118**, e2106744118 (2021).
45. Xie, F., Song, Z., Lian, B. & Bernevig, B. A. Topology-bounded superfluid weight in twisted bilayer graphene. *Phys. Rev. Lett.* **124**, 167002 (2020).
46. Herzog-Arbeitman, J., Peri, V., Schindler, F., Huber, S. D. & Bernevig, B. A. Superfluid weight bounds from symmetry and quantum geometry in flat bands. *Phys. Rev. Lett.* **128**, 087002 (2022).
47. Nelson, D. R. & Kosterlitz, J. M. Universal jump in the superfluid density of two-dimensional superfluids. *Phys. Rev. Lett.* **39**, 1201–1205 (1977).
48. Hofmann, J. S., Berg, E. & Chowdhury, D. Superconductivity, pseudogap, and phase separation in topological flat bands. *Phys. Rev. B* **102**, 201112 (2020).
49. Peri, V., Song, Z.-D., Bernevig, B. A. & Huber, S. D. Fragile topology and flat-band superconductivity in the strong-coupling regime. *Phys. Rev. Lett.* **126**, 027002 (2021).
50. Tovmasyan, M., Peotta, S., Liang, L., Törmä, P. & Huber, S. D. Preformed pairs in flat Bloch bands. *Phys. Rev. B* **98**, 134513 (2018).
51. Mondaini, R., Batrouni, G. G. & Grémaud, B. Pairing and superconductivity in the flat band: Creutz lattice. *Phys. Rev. B* **98**, 155142 (2018).
52. Chan, S. M., Grémaud, B. & Batrouni, G. G. Pairing and superconductivity in quasi-one-dimensional flat-band systems: Creutz and sawtooth lattices. *Phys. Rev. B* **105**, 024502 (2022).
53. Bistritzer, R. & MacDonald, A. H. Moiré bands in twisted double-layer graphene. *Proc. Natl. Acad. Sci. USA* **108**, 12233–12237 (2011).
54. Liu, X. et al. Superconductors, orbital magnets and correlated states in magic-angle bilayer graphene. *Nature* **574**, 653–657 (2019).
55. Yankowitz, M. et al. Tuning superconductivity in twisted bilayer graphene. *Science* **363**, 1059–1064 (2019).
56. Saito, Y., Ge, J., Watanabe, K., Taniguchi, T. & Young, A. F. Independent superconductors and correlated insulators in twisted bilayer graphene. *Nat. Phys.* **16**, 926–930 (2020).
57. Stepanov, P. et al. Untying the insulating and superconducting orders in magic-angle graphene. *Nature* **583**, 375–378 (2020).
58. Liu, X. et al. Tuning electron correlation in magic-angle twisted bilayer graphene using Coulomb screening. *Science* **371**, 1261–1265 (2021).
59. Serlin, M. et al. Intrinsic quantized anomalous Hall effect in a moiré heterostructure. *Science* **367**, 900–903 (2019).
60. Jiang, Y. et al. Charge order and broken rotational symmetry in magic-angle twisted bilayer graphene. *Nature* **573**, 91–95 (2019).
61. Xie, Y. et al. Spectroscopic signatures of many-body correlations in magic-angle twisted bilayer graphene. *Nature* **572**, 101–105 (2019).
62. Choi, Y. et al. Electronic correlations in twisted bilayer graphene near the magic angle. *Nat. Phys.* **15**, 1174–1180 (2019).
63. Nuckolls, K. P. et al. Strongly correlated Chern insulators in magic-angle twisted bilayer graphene. *Nature* **588**, 610–615 (2020).
64. Choi, Y. et al. Correlation-driven topological phases in magic-angle twisted bilayer graphene. *Nature* **589**, 536–541 (2021).
65. Das, I. et al. Symmetry broken Chern insulators and magic series of Rashba-like Landau level crossings in magic angle bilayer graphene. *Nat. Phys.* **17**, 710–714 (2021).
66. Wu, S., Zhang, Z., Watanabe, K., Taniguchi, T. & Andrei, E. Y. Chern insulators, van Hove singularities and topological flat bands in magic-angle twisted bilayer graphene. *Nat. Mater.* **20**, 488–494 (2021).
67. Lu, X. et al. Multiple flat bands and topological Hofstadter butterfly in twisted bilayer graphene close to the second magic angle. *Proc. Natl. Acad. Sci. USA* **118**, e2100006118 (2021).
68. Burg, G. W. et al. Evidence of emergent symmetry and valley Chern number in twisted double-bilayer graphene. Preprint at *arXiv* 2006.14000 (2020).
69. Zou, L., Po, H. C., Vishwanath, A. & Senthil, T. Band structure of twisted bilayer graphene: Emergent symmetries, commensurate approximants, and Wannier obstructions. *Phys. Rev. B* **98**, 085435 (2018).
70. Fu, Y., König, E. J., Wilson, J. H., Chou, Y.-Z. & Pixley, J. H. Magic-angle semimetals. *NPJ Quantum Mater.* **5**, 71 (2020).
71. Liu, J., Liu, J. & Dai, X. Pseudo Landau level representation of twisted bilayer graphene: Band topology and implications on the correlated insulating phase. *Phys. Rev. B* **99**, 155415 (2019).
72. Kang, J. & Vafek, O. Symmetry, maximally localized Wannier states, and a low-energy model for twisted bilayer graphene narrow bands. *Phys. Rev. X* **8**, 031088 (2018).
73. Song, Z. et al. All magic angles in twisted bilayer graphene are topological. *Phys. Rev. Lett.* **123**, 036401 (2019).
74. Po, H. C., Zou, L., Senthil, T. & Vishwanath, A. Faithful tight-binding models and fragile topology of magic-angle bilayer graphene. *Phys. Rev. B* **99**, 195455 (2019).
75. Ahn, J., Park, S. & Yang, B.-J. Failure of Nielsen-Ninomiya theorem and fragile topology in two-dimensional systems with space-time inversion symmetry: application to twisted bilayer graphene at magic angle. *Phys. Rev. X* **9**, 021013 (2019).
76. Bouhon, A., Black-Schaffer, A. M. & Slager, R.-J. Wilson loop approach to fragile topology of split elementary band representations and topological crystalline insulators with time-reversal symmetry. *Phys. Rev. B* **100**, 195135 (2019).
77. Lian, B., Xie, F. & Bernevig, B. A. Landau level of fragile topology. *Phys. Rev. B* **102**, 041402 (2020).
78. Hejazi, K., Liu, C. & Balents, L. Landau levels in twisted bilayer graphene and semiclassical orbits. *Phys. Rev. B* **100**, 035115 (2019).
79. Kang, J. & Vafek, O. Strong coupling phases of partially filled twisted bilayer graphene narrow bands. *Phys. Rev. Lett.* **122**, 246401 (2019).
80. Bulinck, N. et al. Ground state and hidden symmetry of magic-angle graphene at even integer filling. *Phys. Rev. X* **10**, 031034 (2020).
81. Po, H. C., Zou, L., Vishwanath, A. & Senthil, T. Origin of Mott insulating behavior and superconductivity in twisted bilayer graphene. *Phys. Rev. X* **8**, 031089 (2018).
82. Julku, A., Peltonen, T., Liang, L., Heikkilä, T. & Törmä, P. Superfluid weight and Berezinskii-Kosterlitz-Thouless transition temperature of twisted bilayer graphene. *Phys. Rev. B* **101**, 060505 (2020).
83. Hu, X., Hyart, T., Pikulin, D. I. & Rossi, E. Geometric and conventional contribution to the superfluid weight in twisted bilayer graphene. *Phys. Rev. Lett.* **123**, 237002 (2019).
84. Kang, J. & Vafek, O. Non-Abelian Dirac node braiding and near-degeneracy of correlated phases at odd integer filling in magic-angle twisted bilayer graphene. *Phys. Rev. B* **102**, 035161 (2020).

85. Soejima, T., Parker, D. E., Bultinck, N., Hauschild, J. & Zaletel, M. P. Efficient simulation of moiré materials using the density matrix renormalization group. *Phys. Rev. B* **102**, 205111 (2020).
86. Pixley, J. H. & Andrei, E. Y. Ferromagnetism in magic-angle graphene. *Science* **365**, 543 (2019).
87. Xie, M. & MacDonald, A. H. Nature of the correlated insulator states in twisted bilayer graphene. *Phys. Rev. Lett.* **124**, 097601 (2020).
88. Liu, J. & Dai, X. Theories for the correlated insulating states and quantum anomalous Hall effect phenomena in twisted bilayer graphene. *Phys. Rev. B* **103**, 035427 (2021).
89. Cea, T. & Guinea, F. Band structure and insulating states driven by Coulomb interaction in twisted bilayer graphene. *Phys. Rev. B* **102**, 045107 (2020).
90. Da Liao, Y. et al. Correlation-induced insulating topological phases at charge neutrality in twisted bilayer graphene. *Phys. Rev. X* **11**, 011014 (2021).
91. Abouelkomsan, A., Liu, Z. & Bergholtz, E. J. Particle-hole duality, emergent Fermi liquids, and fractional Chern insulators in moiré flatbands. *Phys. Rev. Lett.* **124**, 106803 (2020).
92. Repellin, C. & Senthil, T. Chern bands of twisted bilayer graphene: Fractional Chern insulators and spin phase transition. *Phys. Rev. Res.* **2**, 023238 (2020).
93. Vafek, O. & Kang, J. Renormalization group study of hidden symmetry in twisted bilayer graphene with Coulomb interactions. *Phys. Rev. Lett.* **125**, 257602 (2020).
94. Fernandes, R. M. & Vanderbilt, J. W. F. Nematicity with a twist: Rotational symmetry breaking in a moiré superlattice. *Sci. Adv.* **6**, eaab8834 (2020).
95. Wilson, J. H., Fu, Y., Das Sarma, S. & Pixley, J. H. Disorder in twisted bilayer graphene. *Phys. Rev. Res.* **2**, 023325 (2020).
96. Wang, J., Zheng, Y., Millis, A. J. & Cano, J. Chiral approximation to twisted bilayer graphene: Exact intravalley inversion symmetry, nodal structure, and implications for higher magic angles. *Phys. Rev. Res.* **3**, 023155 (2021).
97. Song, Z.-D., Lian, B., Regnault, N. & Bernevig, B. A. Twisted bilayer graphene. II. Stable symmetry anomaly. *Phys. Rev. B* **103**, 205412 (2021).
98. Bernevig, B. A. et al. Twisted bilayer graphene. V. Exact analytic many-body excitations in Coulomb Hamiltonians: Charge gap, Goldstone modes, and absence of Cooper pairing. *Phys. Rev. B* **103**, 205415 (2021).
99. Codecido, E. et al. Correlated insulating and superconducting states in twisted bilayer graphene below the magic angle. *Sci. Adv.* **5**, eaaw9770 (2019).
100. Roy, B. & Jurčič, V. Unconventional superconductivity in nearly flat bands in twisted bilayer graphene. *Phys. Rev. B* **99**, 121407 (2019).
101. Wang, J., Cano, J., Millis, A. J., Liu, Z. & Yang, B. Exact Landau level description of geometry and interaction in a flatband. *Phys. Rev. Lett.* **127**, 246403 (2021).
102. Lian, B. et al. Twisted bilayer graphene. IV. Exact insulator ground states and phase diagram. *Phys. Rev. B* **103**, 205414 (2021).
103. Zhang, X. et al. Correlated insulating states and transport signature of superconductivity in twisted trilayer graphene superlattices. *Phys. Rev. Lett.* **127**, 166802 (2021).
104. Chen, G. et al. Signatures of tunable superconductivity in a trilayer graphene moiré superlattice. *Nature* **572**, 215–219 (2019).
105. Park, J., Cao, Y., Watanabe, K., Taniguchi, T. & Jarillo-Herrero, P. Tunable strongly coupled superconductivity in magic-angle twisted trilayer graphene. *Nature* **590**, 249 (2021).
106. Classen, L. Geometry rescues superconductivity in twisted graphene. *Physics* **13**, 23 (2020).
107. Su, Y. & Lin, S.-Z. Pairing symmetry and spontaneous vortex-antivortex lattice in superconducting twisted-bilayer graphene: Bogoliubov-de Gennes approach. *Phys. Rev. B* **98**, 195101 (2018).
108. Lopes dos Santos, J. M. B., Peres, N. M. R. & Castro Neto, A. H. Graphene bilayer with a twist: Electronic structure. *Phys. Rev. Lett.* **99**, 256802 (2007).
109. Wang, Z., Chaudhary, G., Chen, Q. & Levin, K. Quantum geometric contributions to the BKT transition: Beyond mean field theory. *Phys. Rev. B* **102**, 184504 (2020).
110. Kitamura, T., Yamashita, T., Ishizuka, J., Daido, A. & Yanase, Y. Superconductivity in monolayer FeSe enhanced by quantum geometry. Preprint at <https://arxiv.org/abs/2108.10002> (2021).
111. Lee, D.-H. Hunting down unconventional superconductors. *Science* **357**, 32–33 (2017).
112. Gallego, S. V., Taseli, E. S., Flor, G., Perez-Mato, J. M. & Aroyo, M. I. Magnetic symmetry in the Bilbao Crystallographic Server: a computer program to provide systematic absences of magnetic neutron diffraction. *J. Appl. Crystallogr.* **45**, 1236–1247 (2012).
113. Alexandradinata, A., Dai, X. & Bernevig, B. A. Wilson-loop characterization of inversion-symmetric topological insulators. *Phys. Rev. B* **89**, 155114 (2014).
114. Ahn, J., Kim, D., Kim, Y. & Yang, B.-J. Band topology and linking structure of nodal line semimetals with  $Z_2$  monopole charges. *Phys. Rev. Lett.* **121**, 106403 (2018).
115. Ünal, F. N., Bouhon, A. & Slager, R.-J. Topological elas class as a dynamical observable in optical lattices. *Phys. Rev. Lett.* **125**, 053601 (2020).
116. Po, H. C., Watanabe, H. & Vishwanath, A. Fragile topology and Wannier obstructions. *Phys. Rev. Lett.* **121**, 126402 (2018).
117. Cano, J. et al. Topology of disconnected elementary band representations. *Phys. Rev. Lett.* **120**, 266401 (2018).
118. Yu, R., Qi, X. L., Bernevig, B. A., Fang, Z. & Dai, X. Equivalent expression of  $\mathbb{Z}_2$  topological invariant for band insulators using the non-Abelian Berry connection. *Phys. Rev. B* **84**, 075119 (2011).
119. Bultinck, N., Chatterjee, S. & Zaletel, M. P. Mechanism for anomalous Hall ferromagnetism in twisted bilayer graphene. *Phys. Rev. Lett.* **124**, 166601 (2020).
120. Bernevig, B. A., Song, Z. D., Regnault, N. & Lian, B. Twisted bilayer graphene. III. Interacting Hamiltonian and exact symmetries. *Phys. Rev. B* **103**, 205413 (2021).
121. Bloch, I., Dalibard, J. & Zwerger, W. Many-body physics with ultracold gases. *Rev. Mod. Phys.* **80**, 885–964 (2008).
122. Giorgini, S., Pitaevskii, L. P. & Stringari, S. Theory of ultracold atomic Fermi gases. *Rev. Mod. Phys.* **80**, 1215–1274 (2008).
123. Törmä, P. & Sengstock, K. (eds) *Quantum Gas Experiments: Exploring Many-Body States* (Imperial College Press, 2015).
124. Lewenstein, M., Sanpera, A. & Ahufinger, V. *Ultracold Atoms in Optical Lattices: Simulating Quantum Many-Body Systems* 1st edn. (Oxford Univ. Press, 2012).
125. Cooper, N. R., Dalibard, J. & Spielman, I. B. Topological bands for ultracold atoms. *Rev. Mod. Phys.* **91**, 015005 (2019).
126. Soltan-Panahi, P. et al. Multi-component quantum gases in spin-dependent hexagonal lattices. *Nat. Phys.* **7**, 434–440 (2011).
127. Tarruell, L., Greif, D., Uehlinger, T., Jotzu, G. & Esslinger, T. Creating, moving and merging Dirac points with a Fermi gas in a tunable honeycomb lattice. *Nature* **483**, 302–305 (2012).
128. Jo, G.-B. et al. Ultracold atoms in a tunable optical kagome lattice. *Phys. Rev. Lett.* **108**, 045305 (2012).
129. Taie, S. et al. Coherent driving and freezing of bosonic matter wave in an optical Lieb lattice. *Sci. Adv.* **1**, e1500854 (2015).
130. Gall, M., Wurz, N., Samland, J., Chan, C. F. & Köhl, M. Competing magnetic orders in a bilayer Hubbard model with ultracold atoms. *Nature* **589**, 40–43 (2021).
131. Sbroscia, M. et al. Observing localization in a 2D quasicrystalline optical lattice. *Phys. Rev. Lett.* **125**, 200604 (2020).
132. Mancini, M. et al. Observation of chiral edge states with neutral fermions in synthetic Hall ribbons. *Science* **349**, 1510–1513 (2015).
133. Stuhl, B. K., Lu, H.-I., Aycock, L. M., Genkina, D. & Spielman, I. B. Visualizing edge states with an atomic Bose gas in the quantum Hall regime. *Science* **349**, 1514–1518 (2015).
134. Ozawa, T. & Price, H. M. Topological quantum matter in synthetic dimensions. *Nat. Rev. Phys.* **1**, 349–357 (2019).
135. O'Riordan, L. J., White, A. C. & Busch, T. Moiré superlattice structures in kicked Bose-Einstein condensates. *Phys. Rev. A* **93**, 023609 (2016).
136. González-Tudela, A. & Cirac, J. I. Cold atoms in twisted-bilayer optical potentials. *Phys. Rev. A* **100**, 053604 (2019).
137. Salamon, T. et al. Simulating twistoronics without a twist. *Phys. Rev. Lett.* **125**, 030504 (2020).
138. Salamon, T., Chhajlany, R. W., Dauphin, A., Lewenstein, M. & Rakshit, D. Quantum anomalous Hall phase in synthetic bilayers via twistoronics without a twist. *Phys. Rev. B* **102**, 235126 (2020).
139. Luo, X.-W. & Zhang, C. Spin-twisted optical lattices: Tunable flat bands and Larkin-Ovchinnikov superfluids. *Phys. Rev. Lett.* **126**, 103201 (2021).
140. Meng, Z. et al. Atomic Bose-Einstein condensate in a twisted-bilayer optical lattice. Preprint at <https://arxiv.org/abs/2110.00149> (2021).
141. Carusotto, I. & Castin, Y. Nonequilibrium and local detection of the normal fraction of a trapped two-dimensional Bose gas. *Phys. Rev. A* **84**, 053637 (2011).
142. Sidorenkov, L. A. et al. Second sound and the superfluid fraction in a Fermi gas with resonant interactions. *Nature* **498**, 78–81 (2013).
143. Ho, T.-L. & Zhou, Q. Obtaining the phase diagram and thermodynamic quantities of bulk systems from the densities of trapped gases. *Nat. Phys.* **6**, 131–134 (2010).
144. John, S. T., Hadzibabic, Z. & Cooper, N. R. Spectroscopic method to measure the superfluid fraction of an ultracold atomic gas. *Phys. Rev. A* **83**, 023610 (2011).
145. Edge, J. M. & Cooper, N. R. Probing ultracold Fermi gases with light-induced gauge potentials. *Phys. Rev. A* **83**, 053619 (2011).
146. Peotta, S., Chien, C.-C. & Di Ventra, M. Phase-induced transport in atomic gases: From superfluid to Mott insulator. *Phys. Rev. A* **90**, 053615 (2014).
147. Rossini, D., Fazio, R., Giovannetti, V. & Silva, A. Quantum quenches, linear response and superfluidity out of equilibrium. *EPL* **107**, 30002 (2014).
148. Krinner, S., Esslinger, T. & Brantut, J.-P. Two-terminal transport measurements with cold atoms. *J. Phys. Condens. Matter* **29**, 343003 (2017).
149. Krinner, S., Stadler, D., Husmann, D., Brantut, J.-P. & Esslinger, T. Observation of quantized conductance in neutral matter. *Nature* **517**, 64–67 (2015).
150. Krinner, S., Stadler, D., Meineke, J., Brantut, J.-P. & Esslinger, T. Superfluidity with disorder in a thin film of quantum gas. *Phys. Rev. Lett.* **110**, 100601 (2013).
151. Pykkönen, V. A. J. et al. Flat-band transport and Josephson effect through a finite-size sawtooth lattice. *Phys. Rev. B* **103**, 144519 (2021).
152. Huhtinen, K.-E. & Törmä, P. Possible insulator-pseudogap crossover in the attractive Hubbard model on the Lieb lattice. *Phys. Rev. B* **103**, L220502 (2021).
153. Chin, C., Grimm, R., Julienne, P. & Tiesinga, E. Feshbach resonances in ultracold gases. *Rev. Mod. Phys.* **82**, 1225–1286 (2010).
154. Mazurenko, A. et al. A cold-atom Fermi–Hubbard antiferromagnet. *Nature* **545**, 462–466 (2017).
155. Dolgirev, P. E. et al. Characterizing two-dimensional superconductivity via nanoscale noise magnetometry with single-spin qubits. *Phys. Rev. B* **105**, 024507 (2022).
156. Tian, H. et al. Evidence for flat band Dirac superconductor originating from quantum geometry. Preprint at <https://arxiv.org/abs/2112.13401> (2021).
157. Jia, Y. et al. Evidence for a monolayer excitonic insulator. *Nat. Phys.* **18**, 87–93 (2022).
158. Wang, P. et al. One-dimensional Luttinger liquids in a two-dimensional moiré lattice. *Nature* **605**, 57–62 (2022).
159. Zhou, H., Xie, T., Taniguchi, T., Watanabe, K. & Young, A. F. Superconductivity in rhombohedral trilayer graphene. *Nature* **598**, 434–438 (2021).
160. Hazra, T., Verma, N. & Randeria, M. Bounds on the superconducting transition temperature: Applications to twisted bilayer graphene and cold atoms. *Phys. Rev. X* **9**, 031049 (2019).
161. Hofmann, J. S., Chowdhury, D., Kivelson, S. A. & Berg, E. Heuristic bounds on superconductivity and how to exceed them. Preprint at <https://arxiv.org/abs/2105.09322> (2021).
162. Topp, G. E., Eckhardt, C. J., Kennes, D. M., Sentef, M. A. & Törmä, P. Light-matter coupling and quantum geometry in moiré materials. *Phys. Rev. B* **104**, 064306 (2021).
163. Chaudhary, S., Lewandowski, G. & Refael, G. Shift-current response as a probe of quantum geometry and electron-electron interactions in twisted bilayer graphene. *Phys. Rev. Res.* **4**, 013164 (2022).

164. Hu, X., Hyart, T., Pikulin, D. I. & Rossi, E. Quantum-metric-enabled exciton condensate in double twisted bilayer graphene. *Phys. Rev. B* **105**, L140506 (2022).
165. Julku, A., Bruun, G. M. & Törmä, P. Quantum geometry and flat band Bose-Einstein condensation. *Phys. Rev. Lett.* **127**, 170404 (2021).

**Acknowledgements**

S.P. and P.T. acknowledge support by the Academy of Finland under project numbers 330384, 336369, 303351 and

327293. B.A.B. acknowledges support from the Office of Naval Research grant no. N00014-20-1-2303 and from the European Research Council (ERC) under the European Union's Horizon 2020 research and innovation programme (grant agreement no. 101020833).

**Author contributions**

All authors have contributed to the writing of the manuscript.

**Competing interests**

The authors declare no competing interests.

**Peer review information**

*Nature Reviews Physics* thanks Wang Yao and the other, anonymous, reviewers for their contribution to the peer review of this work.

**Publisher's note**

Springer Nature remains neutral with regard to jurisdictional claims in published maps and institutional affiliations.

© Springer Nature Limited 2022